UNIVERSITY OF OKLAHOMA

GRADUATE COLLEGE

FRACTURING OF MISSISSIPPI LIME, OKLAHOMA:
EXPERIMENTAL, SEISMIC ATTRIBUTES AND IMAGE LOGS ANALYSES

A THESIS

SUBMITTED TO THE GRADUATE FACULTY

in partial fulfillment of the requirements for the

Degree of

MASTER OF SCIENCE

By

HENRY GEORGE WHITE III
Norman, Oklahoma
2013

FRACTURING OF MISSISSIPPI LIME, OKLAHOMA:

EXPERIMENTAL, SEISMIC ATTRIBUTES AND IMAGE LOGS ANALYSES

A THESIS APPROVED FOR THE
CONOCOPHILLIPS SCHOOL OF GEOLOGY AND GEOPHYSICS

BY

____
Dr. Ze'ev Reches, Chair

____
Dr. Kurt Marfurt

____
Dr. Jamie Rich

Acknowledgements

I wish to thank my advisers Ze’ev Reches and Kurt Marfurt for their patience and wisdom, Shane Matson and Charles Wickstrom of Spyglass Energy LLC as well as the Osage Nation for the data, Bob Davis of Schlumberger for aid in software licensing, Walter Manger for advise on stratigraphy, Michelle Summers, Neil Suneson, and Randy Keller of the Oklahoma Geological Survey for data support, Ben Dowdell, Trey Stearns, Xiaofeng Chen, my family, and my colleagues for geophysical expertise and the AASPI consortium sponsors for financial support. Image log interpretation was done using Schlumberger’s Techlog petrophysical software, while seismic interpretation and visualization as well as the horizon-based curvature used in the clay modeling was done using Petrel Reservoir modeling software. Volumetric attributes were generated using software developed by the AASPI consortium.

TABLE OF CONTENTS

List of Tables

List of Figures

ABSTRACT

Natural fractures are ubiquitous in sedimentary rocks and they strongly affect the quality of oil reservoirs. This study analyzes fracture patterns and fracturing processes in the Mississippian Lime, central US. This unit, which is located in parts of Oklahoma, Kansas, Arkansas and Missouri, includes large unconventional plays of tight limestone, fractured chert, and high-porosity sweet spots of tripolitic chert. It is hypothesized that zones of high curvature computed from 3D seismic data indicate zones of high strain, and can serve as proxies for higher intensity natural fractures.

I test this hypothesis of fracture-curvature relations by conducting a series of wet clay experiments in which I varied the layer thickness and curvature intensity and found that the intensity of fractures and faults mapped on the clay model top surface positively correlates with the curvature intensity. Further, similar correlations were found in my mapping of an exposure of limestone layers of Royer Dolomite, Arbuckle, OK.

Using a 3D seismic survey of ~114 km^2 in Oklahoma, I calculated the curvature attributes as a proxy for strain and an estimation of both fracture orientation and density. I focused on the most positive curvature, k_1 and the most negative curvature, k_2, and then I used image logs in two horizontal wells in the same area, to compare fracture density to the seismic curvature attributes. The analysis showed a positive correlation between three features: (1) the NE-SW trend of the major curvature axes; (2) the trend of the dominant set of natural fractures in the image logs; and (3) the trend of maximum horizontal stress of the current stress state. I concluded that the density of the fractures in the image log is primarily controlled by the lithology, with possible, local enhancement by the curvature zones mapped on the seismic profile analysis.

BACKGROUND

Approach

The presence of natural conductive fractures significantly increases the porosity and permeability of tight reservoirs, and often makes the difference between a commercially productive and non-productive well. The size of these fractures is below the resolution of traditional seismic data, and thus difficult to detect (Al-Dossary and Marfurt, 2006). High fracture density is assumed to correlate with structural curvature because intense curvature indicates intense strain that leads to intense fracturing in brittle rocks (Nelson, 2001). In an outcrop, layer curvatures are manifested by synclinal and anticlinal folds (Figure 1). Seismic structural curvature analysis of the target horizons in the subsurface is used as a proxy for fracture density estimation and orientation (Chopra and Marfurt, 2010).

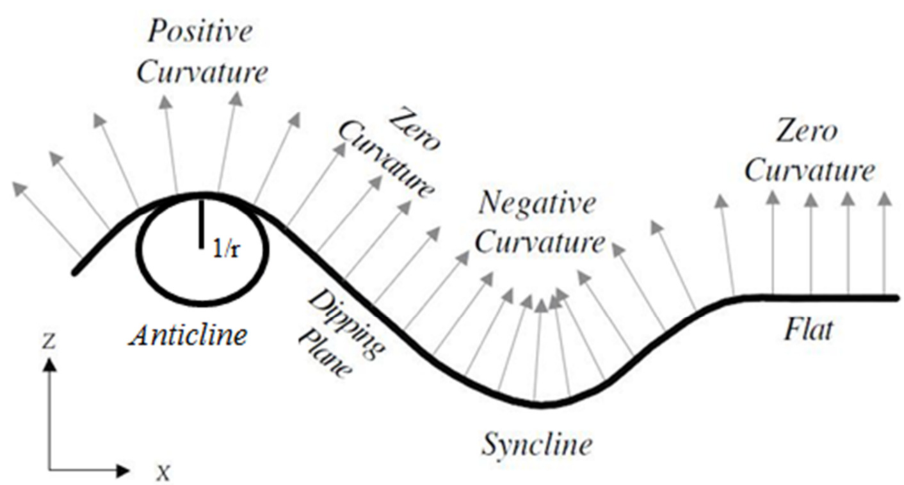

Figure 1. Schematic 2D section of a curved surface. The curvature is $k=1/r$, where r is the radius of the circle tangent at each point of the curve. By convention, the curvature of an anticline is defined to be positive curvature and a syncline to be negative. Planar surfaces have zero curvature (After Roberts, 2001).

Research methods

Laboratory and numerical background

The curvature approach to fracture detection is based on plate bending analysis (Staples, 2011) and outcrop observations (Hennings, 2000; Pearce, 2011). Laboratory plate bending experiments with rocks and elastic material, as well as numerical simulations revealed the stress and strain bending fields (Busetti, 2009). The deformation developed from linear through nonlinear behavior until critical strain at which the plate failed by tensile fractures. The bending intensity is quantified by the curvature, and the relations between curvature and strain for a beam is (after Manaker, 2007),

$$\varepsilon = \frac{h}{2R_c} = k\frac{h}{2}, \qquad (1)$$

where: ε = tensile strain at the convex part of a beam,

h = beam thickness,

R_c = radius of curvature of the beam, and

k = the curvature defined as $k = \frac{1}{Rc}$.

Tensile fractures are most likely to develop in areas with the highest amount of tensile stress, as demonstrated for example, in four-point plate bending experiments of rock beams (Weinberger et al., 1995; Wu and Pollard 1995) and numerical simulations by Busetti (2009). These fractures may be analog to tensile fractures in anticlinal or synclinal features in a natural fold (Lisle, 1994; Staples, 2011). It is expected that when a brittle rock layer in the field is folded into anticlines and synclines, fractures develop in the areas of highest extensional strain in the convex side of the fold.

Clay modeling

The relationships between strain, fracture density, and curvature were investigated in laboratory clay experiments (Staples, 2011; Bose and Mitra, 2010). Clay experiments are used in geostructural modeling because their fault and fracture patterns are similar to fault and fracture pattern in the field, and the clay cakes can be easily deformed by compressional, shear, and tensile loading (Cloos, 1928; Reches, 1988; Tchalenko, 1970). Clay samples have shown the continuous stable growth of faults and fractures (Reches, 1988), and allow the observation of the evolution and mechanics of tectonic deformation (Oertel, 1965; Hoppener et al., 1969; Hildebrandt-Mittlefeldt, 1979; Reches, 1988).

Bose and Mitra (2010) used clay models to analyze fault evolution and patterns during extension. They used a laser scanner to measure the surface of the clay, and to generate a 3D surface model. The structure and density maps of these models showed a listric growth fault develops in two phases (Bose and Mitra, 2010). The early deformation results in the formation of a symmetric graben with symmetrically distributed synthetic and antithetic faults (Bose and Mitra, 2010). Increasing extension results in the coalescence of some of the synthetic normal faults to form a major listric fault (Bose and Mitra, 2010). Once this major fault has formed the structure is transformed into a half graben with a symmetric rollover structure (Bose and Mitra, 2010). After this phase, the formation of new synthetic faults was limited to accommodate synthetic shear; however antithetic faults continued to develop and accommodate the deformation of the hanging wall (Bose and Mitra, 2010).

In a series of clay modeling above compressional and extensional faults, Staples (2011) found a clear positive relationship between fracture intensity and curvature (Figure 2). The onset of fracturing did not occur at the same curvature value in the different runs, due to differences in horizontal strain throughout the three experiments (Staples, 2011).

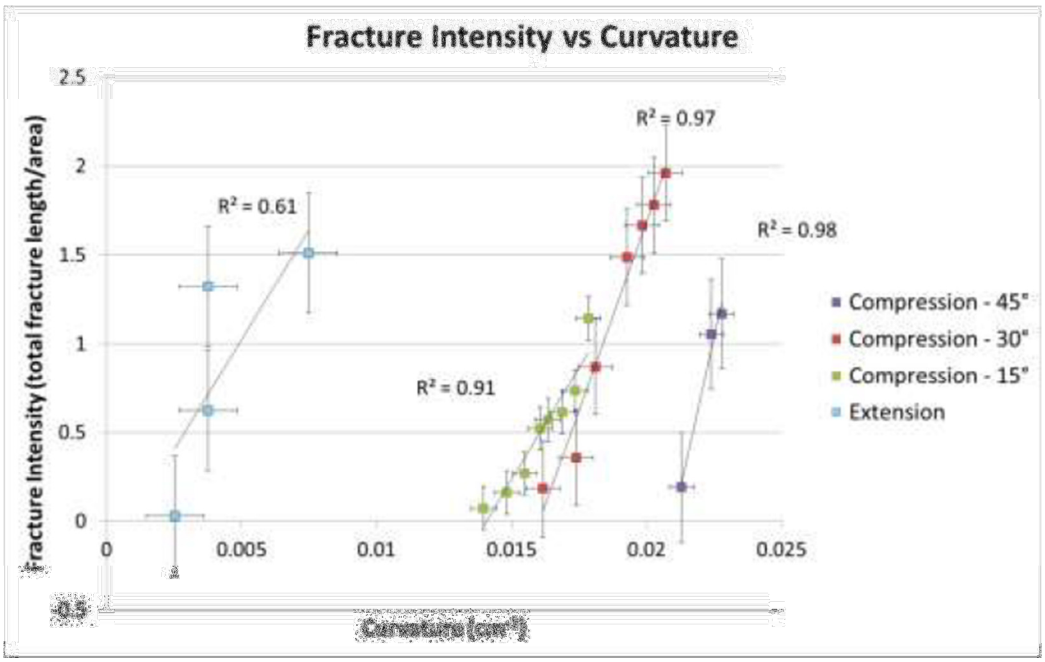

Figure 2. Experimental relationship between fracture intensity in clay cake models above four inclined, basement faults (Staples, 2011).

Curvature analysis in seismic profiles

Curvature is used as a proxy for elevated local strain in the subsurface and indicative of areas suspected for high fracture intensity (Hart, 2002; Sigismondi, 2003; Chopra and Marfurt, 2007). Defining curvature along a 3D horizon requires an approximation method that will fit a quadratic surface of the form

$$z(x,y) = ax^2 + cxy + by^2 + dx + ey + f \qquad (2)$$

where: $z(x,y)$ is the quadratic surface (Roberts, 2001; Chopra and Marfurt, 2007). In 3D, one can fit two intersecting circles having orthogonal geometry with an axis at that intersection that is perpendicular to a plane, tangent to the surface (Roberts, 2001; Sigismondi, 2003; Chopra and Marfurt, 2007). The first circle is adjusted to a point where its radius is the smallest is defined as k_{max} and the second circle, perpendicular to the first and always having the largest radius, is defined as k_{min} (Roberts, 2001; Chopra and Marfurt, 2007). The analysis continues by first calculating the mean curvature, the Gaussian curvature, and finally uses those to calculate the most-positive and most-negative principal curvatures (Chopra and Marfurt, 2007):

$$k_{\mathrm{mean}} = [a(1 + e^2) + b(1 + d^2) - cde]/(1 + d^2 + e^2)^{3/2}, \tag{3}$$

$$k_{\mathrm{Gauss}} = (4ab\text{-}c^2)/(1 + d^2 + e^2)^2 , \tag{4}$$

$$k_1 = k_{mean} + (k_{mean}{}^2 + k_{\mathrm{Gauss}})^{½}, \text{ and} \tag{5a}$$

$$k_2 = k_{mean} - (k_{mean}{}^2 - k_{\mathrm{Gauss}})^{1/2}, \tag{5b}$$

In general, anticlinal and domal features will give rise to most-positive curvature k_1 anomalies while synclinal and basinal features will give rise to most negative curvature, k_2, anomalies. These curves can be related to geologic structural and stratigraphic features (Chopra and Marfurt, 2007) (Figure 3).

The hypothesis of fracture-curvature association can be tested in the subsurface by measurement of fractures in borehole image logs, which can then be compared to k_1 and k_2 curvature zones mapped on seismic profiles (Staples, 2011). As many fractures and fracture swarms are sub-vertical (Nelson, 2001), and as fractures are frequently bounded by lithological contacts (Nelson, 2001), better statistical sampling of such fractures can be obtained in image logs in horizontal wellbores. This was the approach in the present study.

Few publications report the use of image logs in horizontal wellbores with seismic data. Ericsson et al. (2010) analyzed a 3D seismic survey and approximately ten miles of image logs of the Late Cretaceous Ilam Formation of the Arabian Gulf's Fateh Field. It was shown that high-curvature areas accounted for 68%

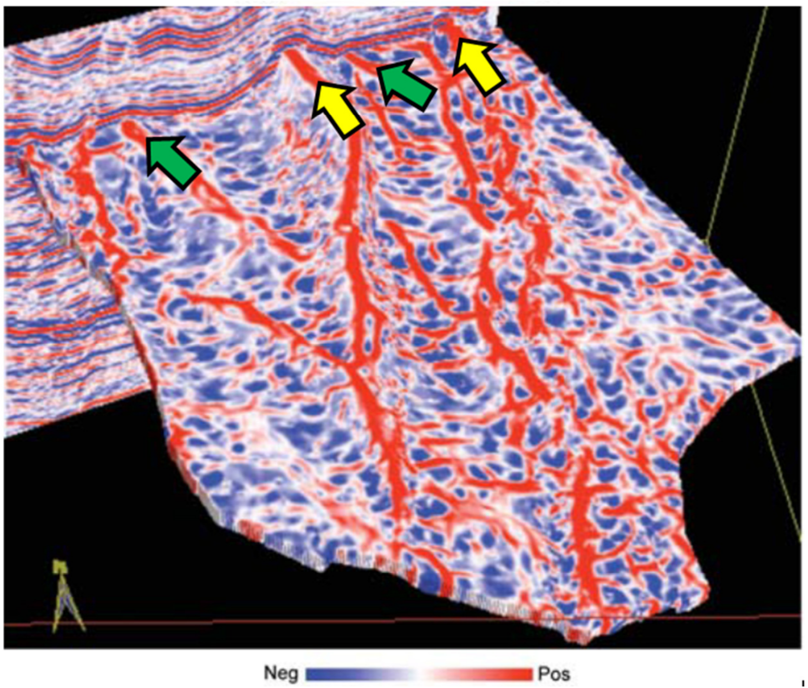

Figure 3. A 3D seismic survey displaying a horizon slice through the most-positive curvature volume and the vertical slice through seismic amplitude. Notice the seismic signatures corresponding to faults or large fracture zones as indicated with yellow arrows. The green arrows simply indicate undulations on the seismic reflections corresponding to fractures (After Chopra and Marfurt., 2007)

of the mapped fractures, also probed the important factor of facies and grain size distribution, observing that 62% of fractures occurred in grain-supported facies as opposed to matrix-supported facies. In addition they found the fractures in grain-supported facies are more than four times wider than those in the matrix-supported facies (Ericsson et al., 1998). The predominant fracture type was found to be hairline macrofractures striking parallel to the present-day maximum principal horizontal stress. Fault patterns and structural curvature also follow this trend in the study area, striking parallel to the present-day maximum principal horizontal stress.

Staples (2011) examined the relationship between curvature zones mapped in a 3D seismic survey (pre-stack time migrated) that covered ~23 km^2, and fracture density determined in image logs of seven horizontal wellbores. The work was conducted in the Late Ordovician to Early Devonian Hunton Limestone reservoir on the Central Platform in Oklahoma, USA. Staples (2011) found a positive correlation between fracture density and k_1 most positive curvature in 5 out of the 7 wells (Figure 4).

Hunt et al. (2010) studied the Nordegg Formation in Alberta, Canada, where fracture density was measured in two horizontal wells using image logs and microseismic "events" in one well during a microseismic experiment. Hunt binned the image log data in 32 m bins to visualize the fracture density on the seismic scale and demonstrated that curvature and AVAz (amplitude variation with azimuth) is a good predictive tool for fracture density (correlation coefficient of 0.74) (Figure 5).

Hennings et al. (2000) analyzed the relationship between fracture density and curvature in the Frontier Formation in the Oil Mountain anticline, Wyoming. They found that curvature increase correlates with fracture intensity increase. Pearce et al. (2011) mapped fractures and curvature using LIDAR at several sites in the United Kingdom, and found poor correlations for the folds studied, all of the fracture spacing distributions showed an exponential distribution, and no significant correlation between fracture density and surface curvature was observed.

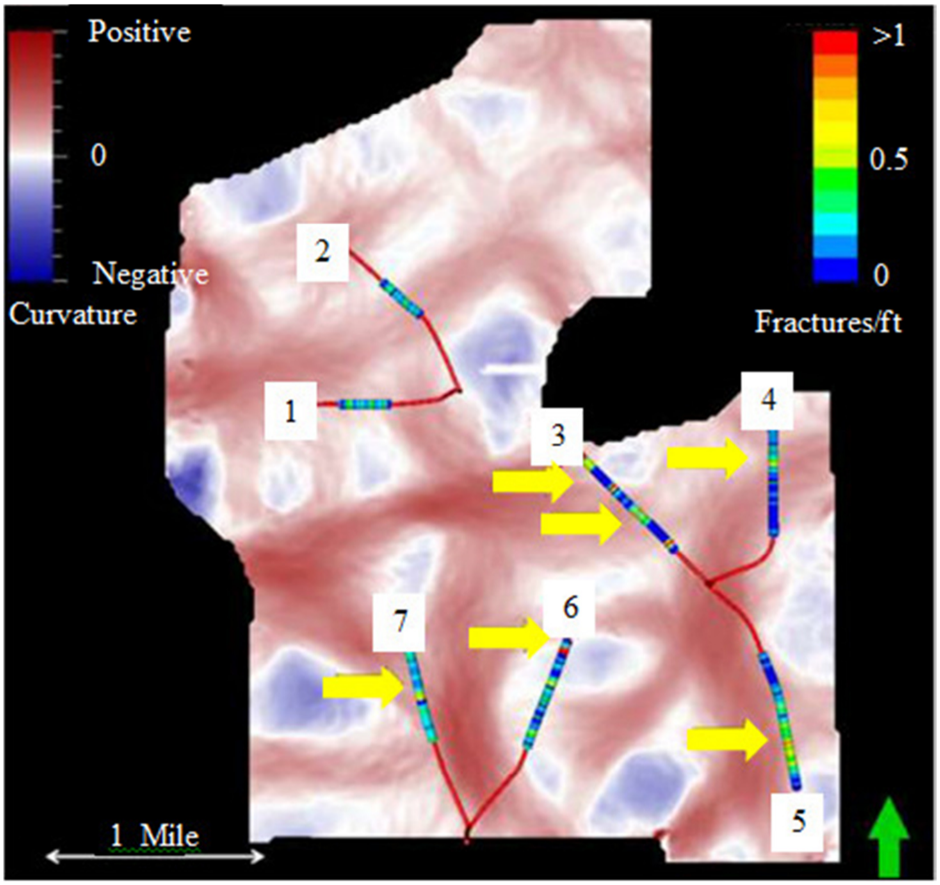

Figure 4. Horizon slice along the top Hunton Group through the k_1 most positive curvature volume. Positive structures (red) visually correlate (yellow arrows) to high fracture density in Wells 3 – 7 (After Staples, 2011).

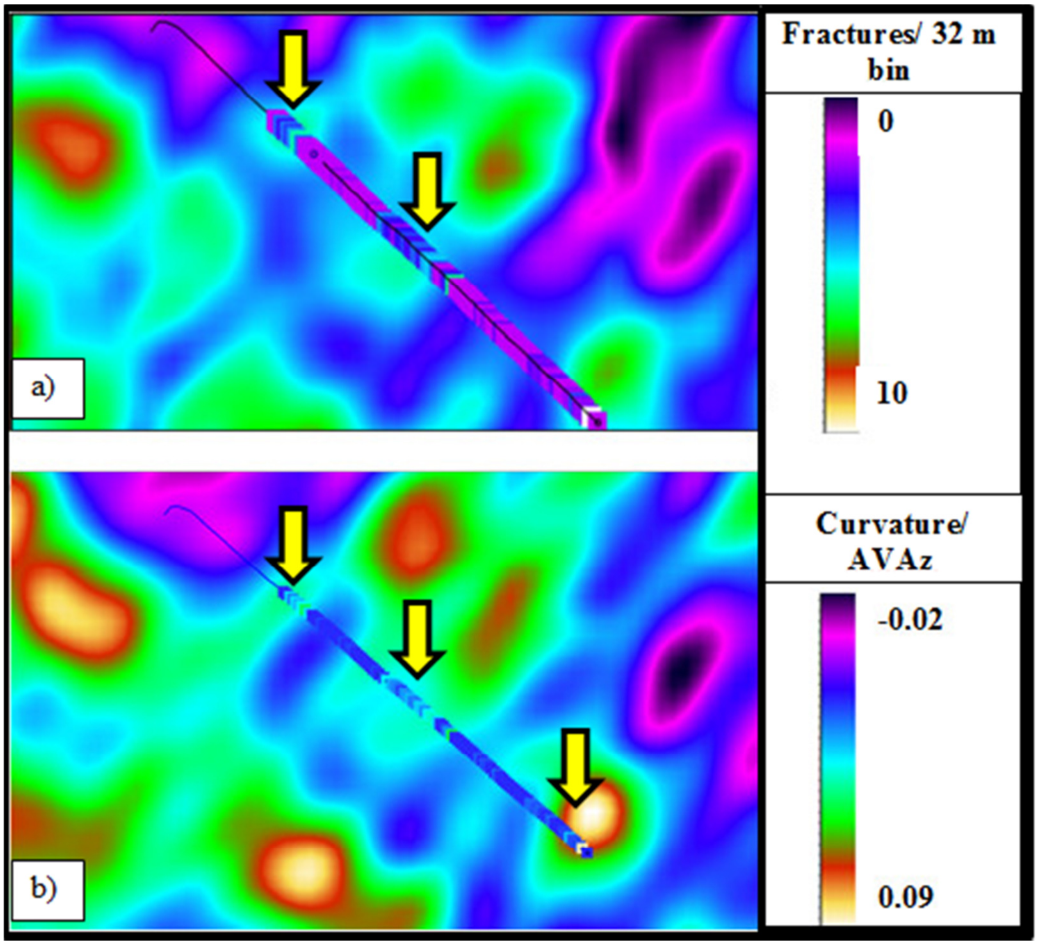

Figure 5. Map of curvature with fracture density in fractures per 32m bin measured along (a) well A and (b) well B. Horizon slice through a volume computed by linearly combining AVAz intensity and curvature. Higher intensity of fractures is shown by warmer colors while lower intensity of fractures is shown by cooler colors. Higher intensity of curvature/AVAz is shown by warmer colors while lower intensity of fractures is shown by cooler colors. Yellow arrows show positive correlations between fracture density and curvature (After Hunt et al., 2010).

PRESENT WORK

Approach

My study combines laboratory clay modeling, outcrop characterization, horizontal image log interpretation, and 3D seismic attribute analysis. The main objective is to delineate natural fractures in the Mississippian Limestone of Osage County, Oklahoma. I use symmetric clay models to examine the relationship between curvature and fracture intensity and the effect of bed thickness on fracture distribution. I also examined a layered limestone outcrop including measurements of layer thickness, curvature, and fracture intensity. Using image logs in two horizontal wellbores, I examine the relations between open fractures and the horizontal stress, lithology, and curvature.

The study is organized in four parts. I begin with a description of the clay modeling experiment and the resulting correlation of fractures to curvature. This is followed by outcrop observations using photographs to characterize fractures and curvature. I continue with an interpretation using volumetric curvature attributes of a 3-D seismic survey in Osage County, Oklahoma. With this framework established I pick and clarify individual fractures on image logs in horizontal wellbores, and convert to fracture density to be viewed at the seismic scale. These measures are then visually and numerically correlated to generate a fracture prediction away from the well logs. I discuss the strengths and weaknesses of this workflow with recommendations for data acquisition and analysis.

Clay modeling

Set-up

The experimental apparatus used for clay modeling has one stationary arm and one moving arm, positioned parallel to each other on top of a horizontal table (Figure 6). The moving side can cause sample extension or shortening at velocities of 0.100 cm/min. The clay cakes were placed on a PMMA (polymethyl methacrylate) plate with dimensions of 24.1 cm by 15.2 cm and 0.075 cm thick. The PMMA plate was placed between the apparatus arms (Figure 6). The surface of the PMMA plate was covered with a 40-grit coarse grained sandpaper to keep the clay cake attached to the plate. The rectangular clay cake has dimensions of 1, 2, 3 cm thick, 10 cm wide, and 18 cm long. The clay has a density of 1.22 g/cm^3. The clay is turned in a Bluebird clay mixer for a minimum of five minutes to ensure a uniform consistency throughout the clay cake. The clay cakes were molded by hand using a trowel in a manner such that air pockets are kept to a minimum and the surface of the cake is smooth, level, and free of cavities. I conducted three compressional experiments at shortening rate of 0.100 cm/min. Over the duration of each experiment, the run was stopped every 1 minute for data collection including sample photography (side, top, and oblique views), and a laser scan with a 75 DPI (~0.4 mm point density) forming a 34.2 by 25.6 cm gridded elevation map. The fracture count and fracture length was interpreted on these images.

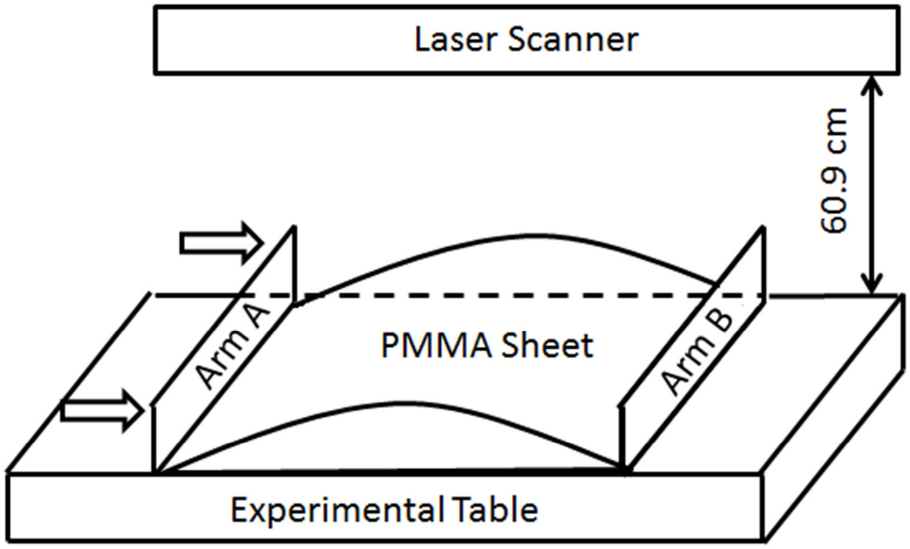

Figure 6. Setup used in clay modeling experiments. Arm B remains stationary while Arm A moves towards it and shortening the PMMA sheet that flexes symmetrically.

Data Collection

The general curvature of the clay cake was calculated from the side view photo of the experiment (Figure 7). Curvature calculation at each interval was calculated by using the second derivative of the polynomial equation calculated from the curve traced along the edge of the PMMA sheet on the side view photo at each interval. The side view photo at 3 minutes (displacement = 0.300 cm) is shown in Figure 7 and a graph over the duration of the experiment is shown in Figure 8.

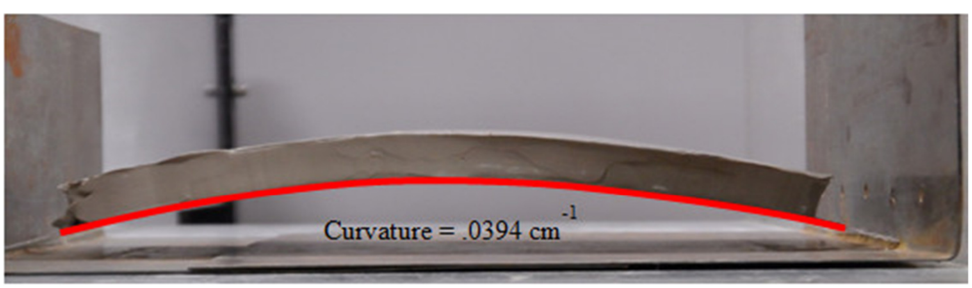

Figure 7. Average curvature of the red line traced along the edge of the PMMA sheet is calculated by using the second derivative of the polynomial equation calculated from the curve traced along the edge of the PMMA sheet on the side view photo at each interval.

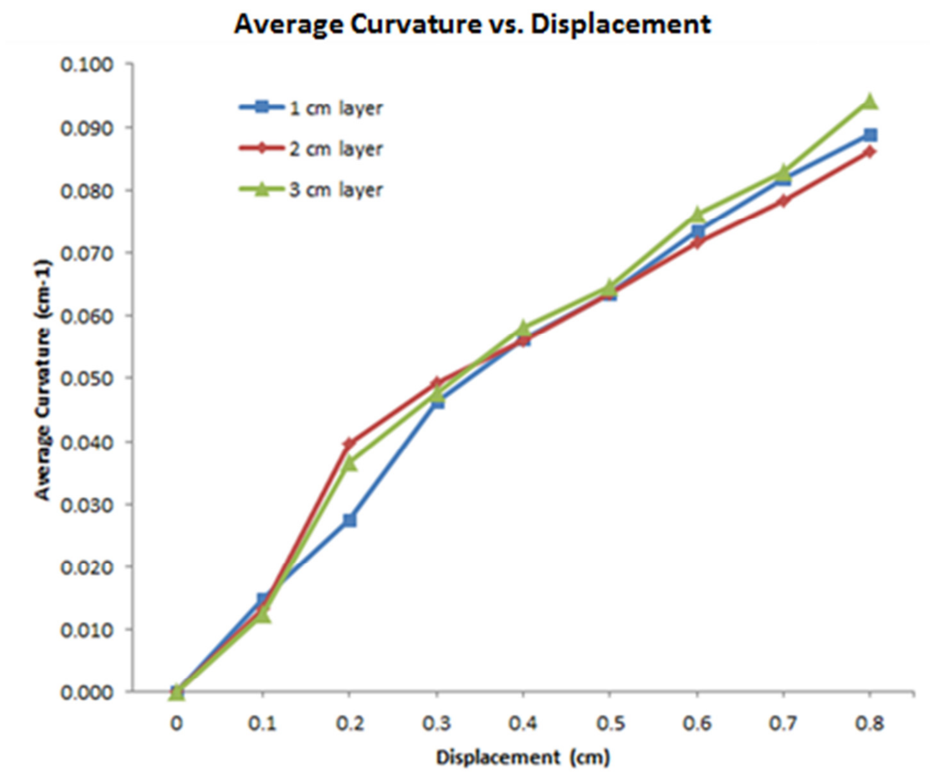

Figure 8. Average curvature of the PMMA plate in 1 cm, 2 cm, and 3 cm experiments as function of the horizontal displacements in the three experiments.

As the PMMA plate is shortened, it buckles and extends the overlying clay cake. This extension led to the development of a system of faults and fractures. The 1D estimation of fracture intensity was determined by using a scan line (Figure 9).

After Sagy and Reches (2006) the intensity is defined as

$$D_{1D} = h/S \qquad (6)$$

where: D_{1D} is the 1D joint (or fracture) intensity, h = the thickness of the layer, and S = the mean distance between fractures (cm). I digitized a photograph to calculate 2D fracture intensity to calculate the fracture intensity in the sample area (Figure 10). The experimental results of the fracture intensity calculation are displayed in Table 1 and Figure 9.

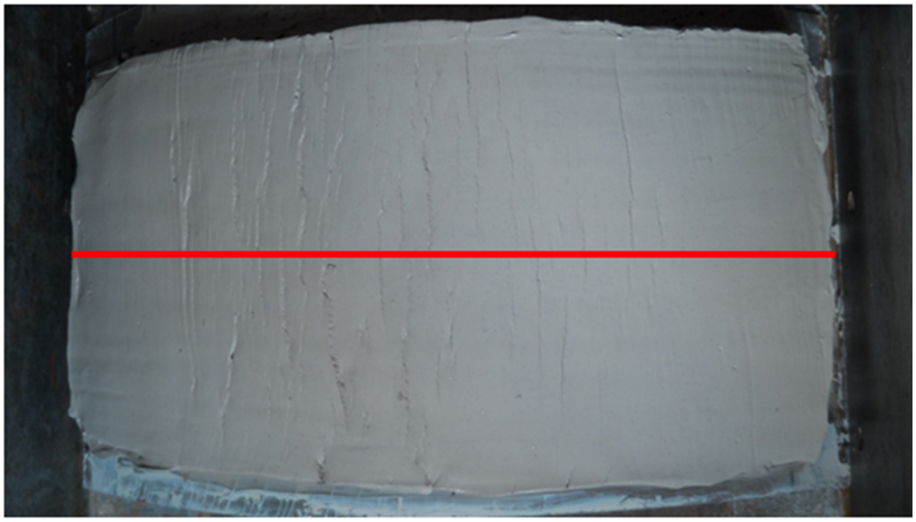

Figure 9. Photo of top of clay cake used in measuring fracture intensity. Red line represents a scan line used to measure mean fracture spacing with fracture intensity = clay cake thickness/average number of fractures per unit of length.

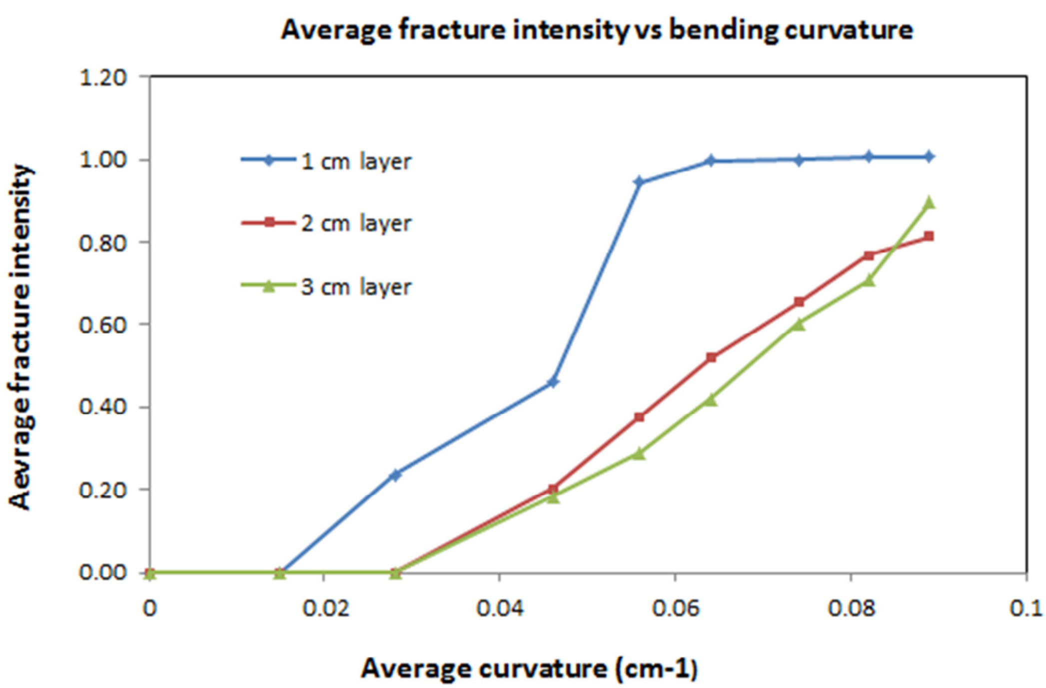

Figure 10. Average fracture intensity vs PMMA curvature in experiments of 1 cm, 2 cm, and 3 cm layer thickness.

The 2D fracture intensity, D_{2D} can be calculated from a map of fractures, as observed on top of a layer (Sagy and Reches (2006) or the top of a clay cake (Figure 11). In this case, the mean fracture density, 1/S, is calculated as the mapped area, A, divided by the total length of the fractures, L_f, and the fracture intensity is

$$D_{2D} = h / S = h / (A / L_f) \quad (7)$$

where D_{2D} = Fracture Density, h = layer thickness, L_f = cumulative length of the fractures, and A= mapped area. The experimental results of the fracture density calculations are displayed in Table 2 and Figure 12.

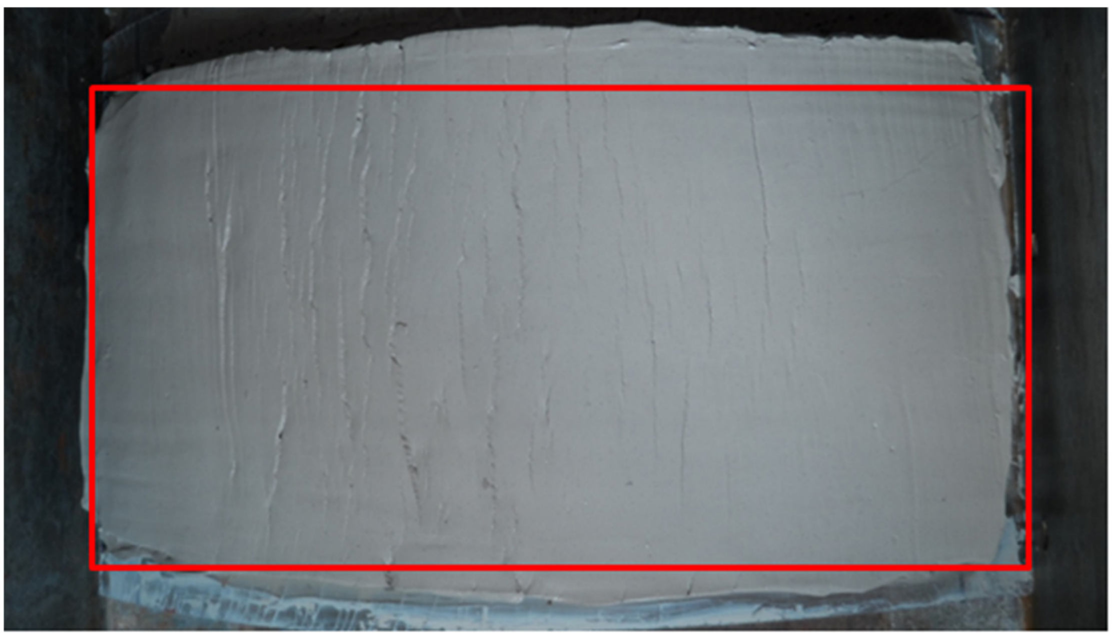

Figure 11. Photo of top of clay cake used in measuring fracture density. Red box represents fracture sampling area used to calculate fracture density where fracture density = thickness of clay cake / ((length of fractures x number of clusters) per unit of area).

Table 1. Fracture intensity vs average curvature of the PMMA in 1, 2, and 3cm experiments.

Time	Displacement (cm)	Fracture Intensity 1 cm	Fracture Intensity 2 cm	Fracture Intensity 3 cm
2	0.2	0.24	0.00	0.00
3	0.3	0.46	0.20	0.18
4	0.4	0.94	0.38	0.29
5	0.5	1.00	0.52	0.42
6	0.6	1.00	0.65	0.60
7	0.7	1.01	0.77	0.71
8	0.8	1.01	0.81	0.90

Table 2. Fracture density vs average curvature of the PMMA in 1, 2, and 3cm experiments.

Time	Displacement (cm)	Fracture Density 1 cm	Fracture Density 2 cm	Fracture Density 3 cm
2	0.2	0.09	0.00	0.00
3	0.3	0.38	0.15	0.25
4	0.4	0.50	0.24	0.38
5	0.5	0.71	0.35	0.57
6	0.6	0.94	0.59	0.83
7	0.7	1.01	0.98	1.12
8	0.8	1.09	1.21	1.28

I used a high definition laser scanner to measure the 3D geometry of the top surface of the clay cake. The scans were recorded at 1 minute intervals throughout each experimental (Figure 13).

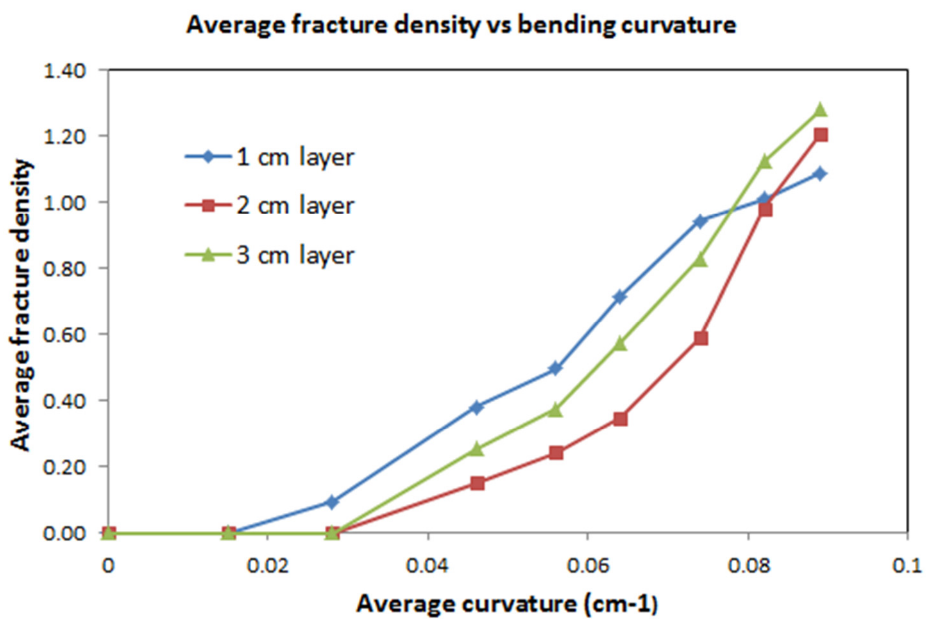

Figure 12. Graph of average fracture density vs average curvature of the PMMA in 1cm, 2cm, and 3cm experiments.

.

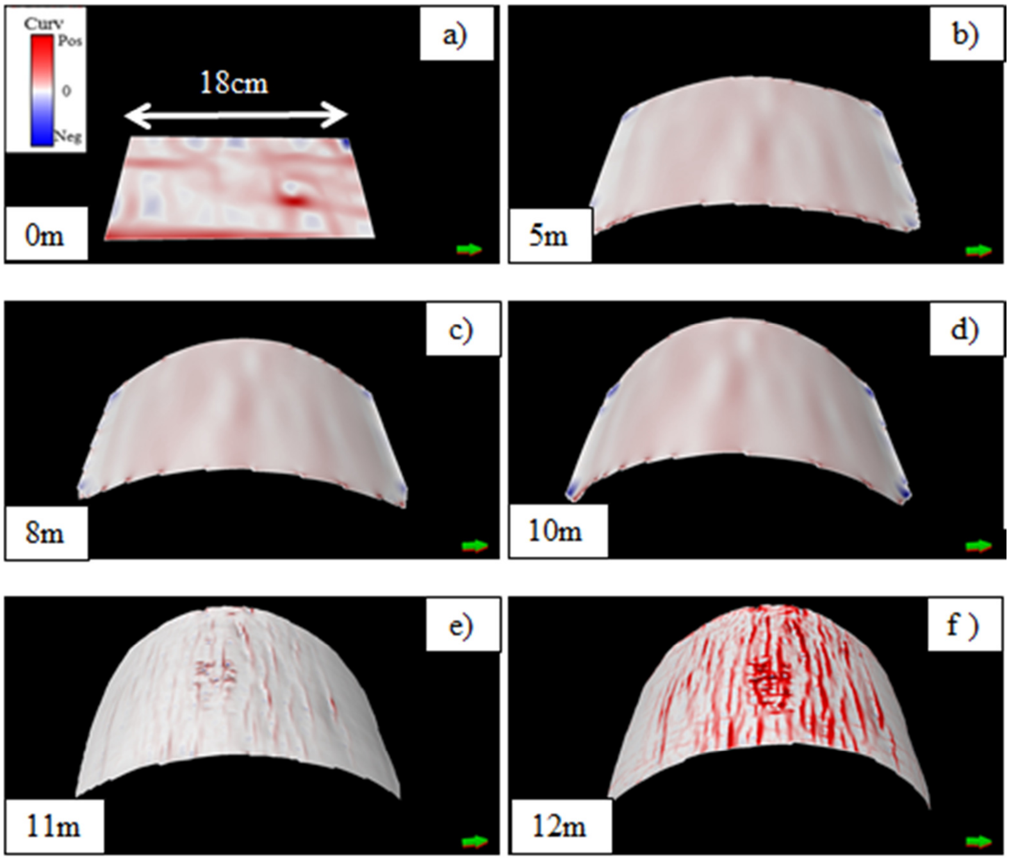

Figure 13. Positive curvature extracted from a clay model's surface at selected intervals (in minutes designated in lower left hand box).

Synthesis

Shortening vs plate curvature: Curvature of the PMMA plate in all clay modeling experiments increased as horizontal shortening increased regardless of clay thickness (Fig. 6, 7).

Fracture Intensity (1D): The experiments show linear relation between curvature and fracture intensity. The parameter indicates the stage of fracture nucleation, and it apparently depends on the thickness of the clay cake. Fracturing initiated earlier in the $h = 1$ cm experiment in which the first fractures appeared at curvature of ~ .015 cm^{-1}. The $h = 1$ cm experiment also seems to reach fracture saturation when it slope decreases to zero, between curvature values of 0.056 cm^{-1} and 0.064 cm^{-1} (Fig. 10), whereas it did not reach zero slope in the other two runs. The experiments with thicker clay, $h = 2$, 3 cm, displays similar trends, initiating at the same curvature, and having similar slopes. Based on the above, it seems that thinner layers reach a critical strain and maximum fracture density before thicker layers.

Fracture Density (2D): Fracture density experiments using clay models show a linear relationship between curvature and fracture density. Fracture length increased at the highest rate in last half of the experiment in the 1cm, 2cm, and 3cm layer experiments. This can be observed in Figure 12 where the lines slope increases after curvature values of ~0.056 cm^{-1} in the 1cm experiment and ~0.065 cm^{-1} in the 2cm and 3cm experiments. This is because the strain needed to propagate the fracture at the tip of the fracture is less than the strain needed for the origination of a new fracture.

Curvature Attribute Analysis: To calculate curvature using the laser scans of the clay cakes top surface I import them into Petrel Interpretation software as an XYZ point file. I create a 25 X 25 pixel resolution gridded surface from the XYZ point file. From this I extract the positive and negative surface curvatures. The laser scans of the experiments (Figures 13, 15,16) display two scales: (1) A large scale positive curvature is dictated by the PMMA base and it is the same for all experiments (Fig. 8,14); and (2) A finer scale negative curvature that represents the local distortion of the clay cake by the fractures and faults (Figure 14, 15). I found above that the total fracture intensity is related to the large scale curvature (Figure 14), whereas the fine scale curvature was higher in magnitude and delineated the edges of the faults and fractures (Figure 13 e-f, 14). It highlights the faults accurately when compared to the photos of the clay cake. Corendering positive and negative curvature gives a complete view of the faulted surface (Figure 16).

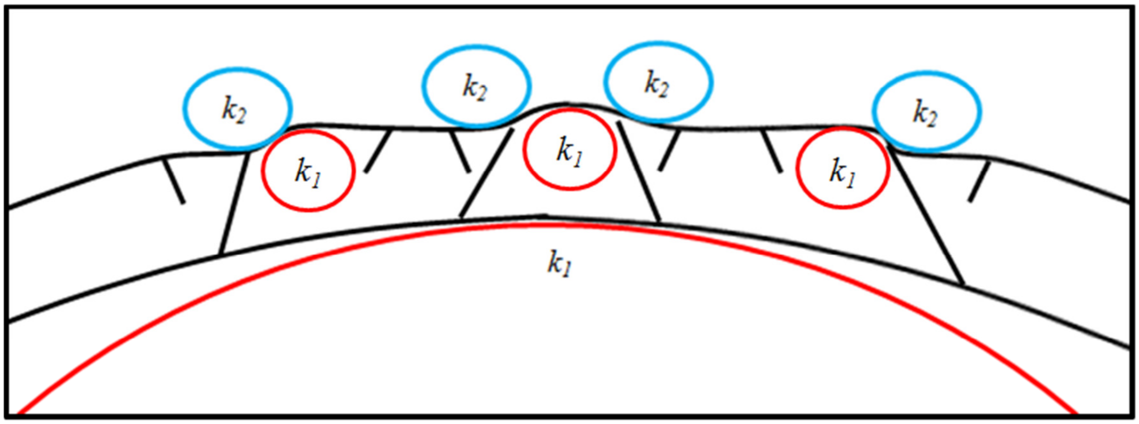

Figure 14. Conceptual diagram showing how curvature attributes manifest on the surface of the clay cake. The black lines show the deformed clay cake with faults and fractures. The red circle is the large scale positive curvature (k_1) of the clay cake dictated by the concave flexure in the PMMA which can be detected early in the experiment. The smaller red and blue circles are fine scale positive (k_1) and negative curvature (k_2) which initiate later in the experiment in convex areas created by displacement along faults.

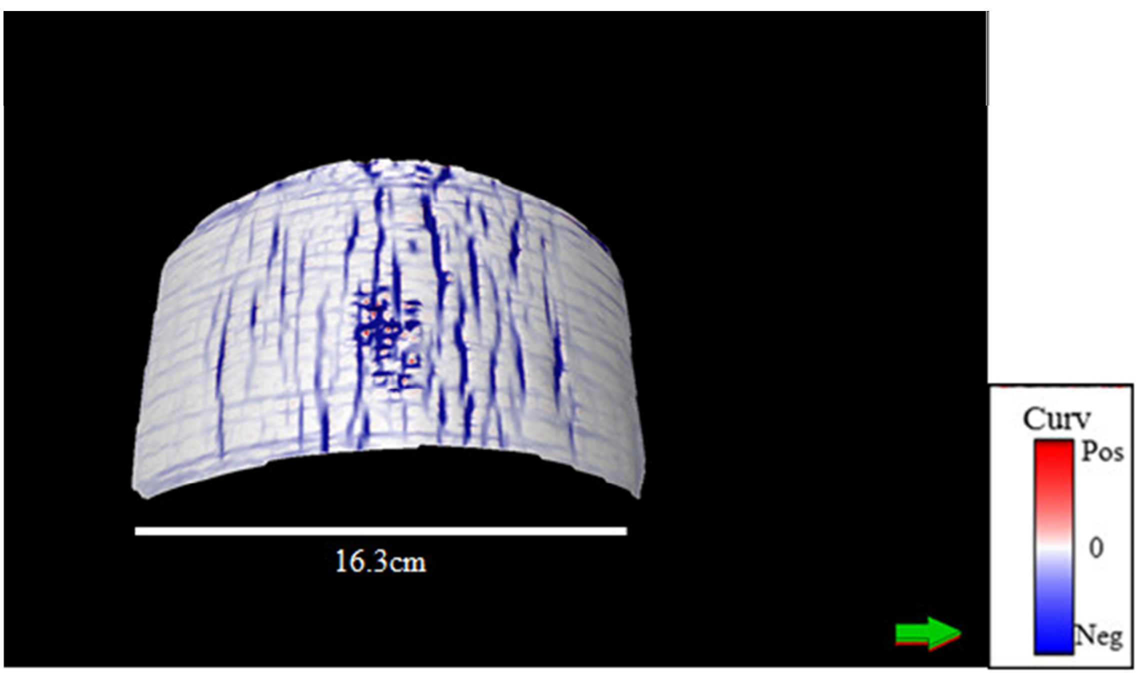

Figure 15. k_2 most negative curvature extracted from surface iteration pictured in Figure 13.

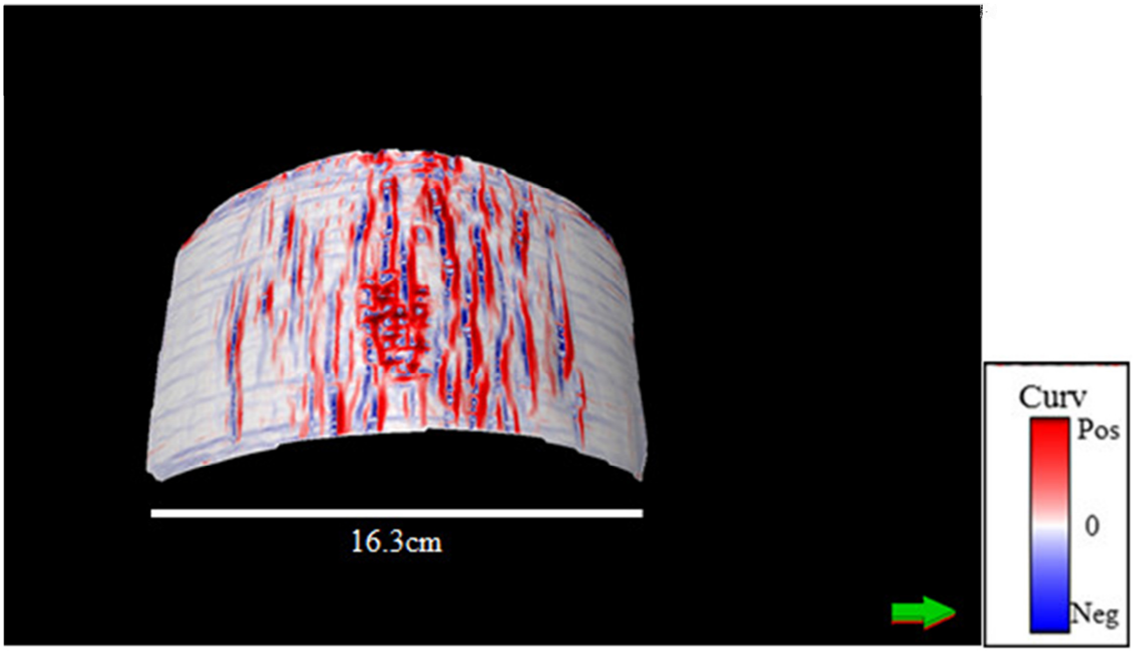

Figure 16. Co-rendered k_1 positive and k_2 negative curvature corresponding to the photo in Figure 13.

Field analysis, Arbuckle Mountains, Oklahoma

I examined the fracture densities in a road cut outcrop of the base of the Royce Dolomite member of the Late Cambrian-Ordovician Arbuckle Group, Arbuckle Mountains, OK (Figure 17). The outcrop is ~ 64 m long and an ~ 8 m average height, road cut along Hwy 35 with blasting boreholes at ~ .61 m spacing; the dynamite blasting fractures could be distinguished from the natural fractures. The outcrop displays a series of reverse and oblique slip faults that probably formed during the Ouachita orogenic event in the late Pennsylvanian ~300 million years ago. I focused on areas of intensely fractured rock in flexed areas. The outcrop consists of alternating packages of thin (.9525 – 5.08 cm) dolomite mudstone beds to massive (165.1 cm) beds of carbonate wackestone. The formation is dolomitized.

Faults A, B, and C in Figure 18 are low angle thrust faults that merge into thin ductile beds ranging in thickness from .58 cm to 10.4 cm. Evidence of displacement is demonstrated by slickensides in Figure 19b. Faults D, E, and F in Figure 18 are high angle reverse faults, and faults G and H in Figure 18 are oblique slip faults antithetic to fault F. Figure 20 shows strike slip striations along fault H.

A plot of the plunge and trend of faults on a Rose/Schmidt diagram is displayed in Figure 21. Two sets of faults can be observed, the primary reverse faults trending NNW-SSE plunging SW at low angles and a secondary conjugate set consisting of a NW-SE oblique slip fault plunging steeply SW and NE-SW oblique slip fault plunging steeply SE.

I examine the fracture-curvature relationship at two small areas of this outcrop. A close up view of Location 1 (Figure 22) displays the termination zone of a thrust fault with intensely fractured region of relatively high curvature (Figures 22-24). Similar association is found at location 2 (Figure 25) that displays a thrust fault with an area of higher curvature and intensely fractured zone in the foot wall. Note the areas an equal distance from the fault on the other side exhibit lower fracture density above areas of lower curvature.

These observations in < 10 m high outcrop are below seismic resolution. The seismic two way travel time (TWT) for an outcrop of this scale, the average distance through the outcrop two ways (18 m) and an interval velocity of 4,572 m/s:

$$TWT = 2h \,/\, V_{avg} \tag{8}$$

where: TWT = two way travel time

h = height of the outcrop

V_{avg} = average velocity

This gives the outcrop a TWT isochron of 4 ms at 9 ft. For maximum wave frequency of 100 Hz during seismic acquisition, the wavelength is 47 m. Thus, only faults larger than 47 m long in the Z direction could be resolved in standard seismic survey. The faults in the studied outcrop are likely to display curvature increase, but could not display an offset in amplitude (Figure 26).

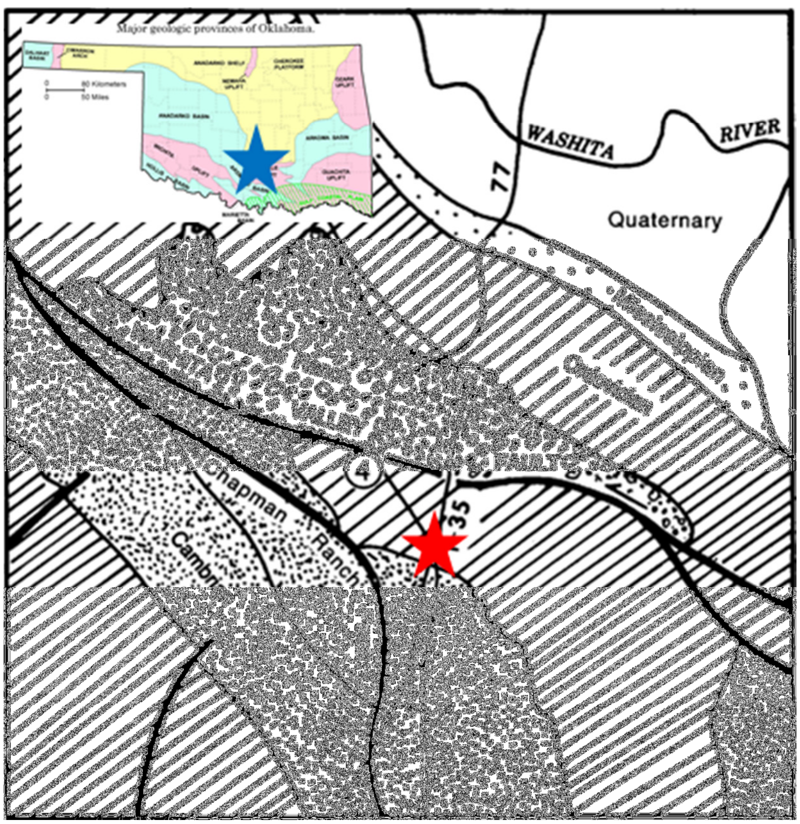

Figure 17. Generalized map of the Arbuckle Mountains (Modified from Brown and Grayson, 1985).. The outcrop study location is designated by a red star. Inset shows the geologic provinces of Oklahoma and the Arbuckle Mountains is shown by a blue star (Johnson, 2008).

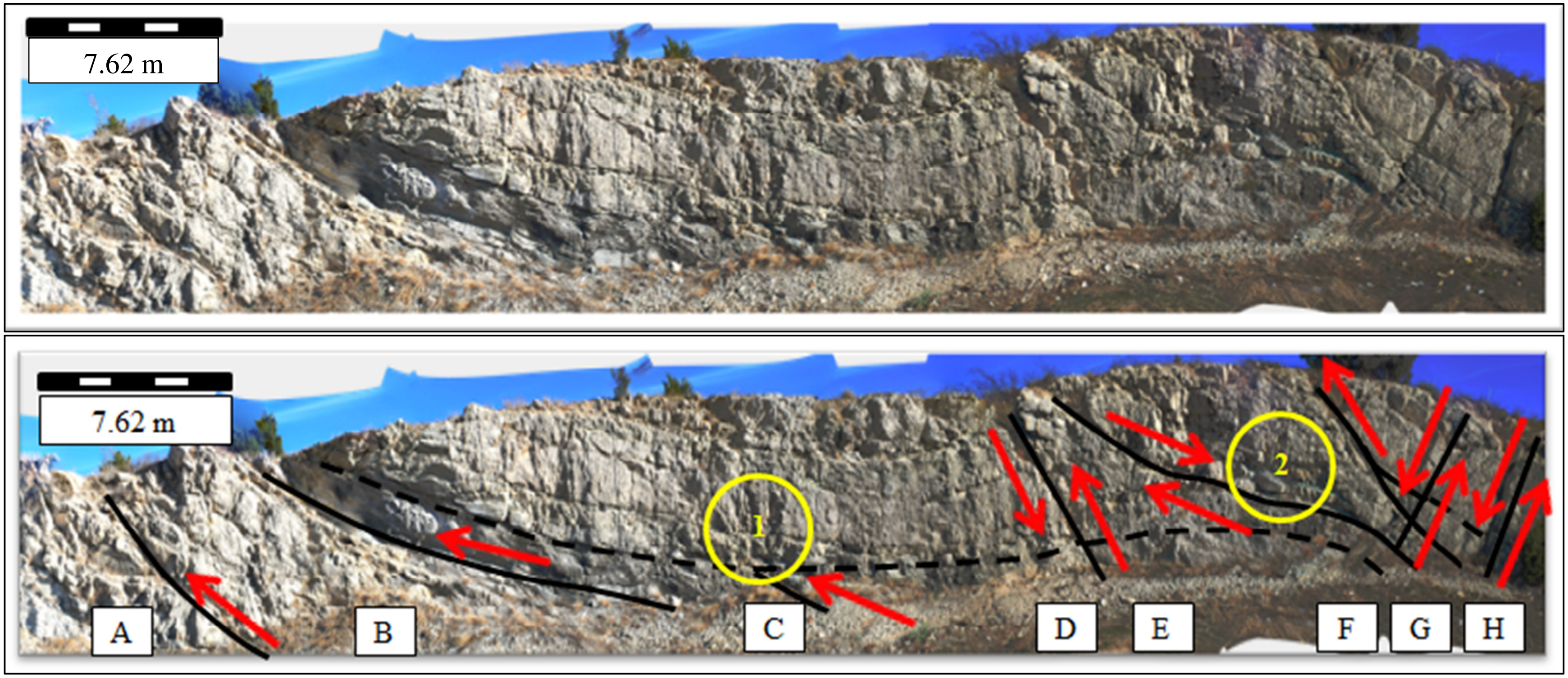

Figure 18. Top. Panoramic photo of Royce Dolomite. Bottom. Interpreted photo; labeled solid black line-fault traces; red arrows-relative fault displacements; dotted black line- detachment zone along bedding surfaces; numbered yellow circles- locations of fracture characterization. Location 1 is an area of a failed thrust ramp and location 2 is a high curvature area.

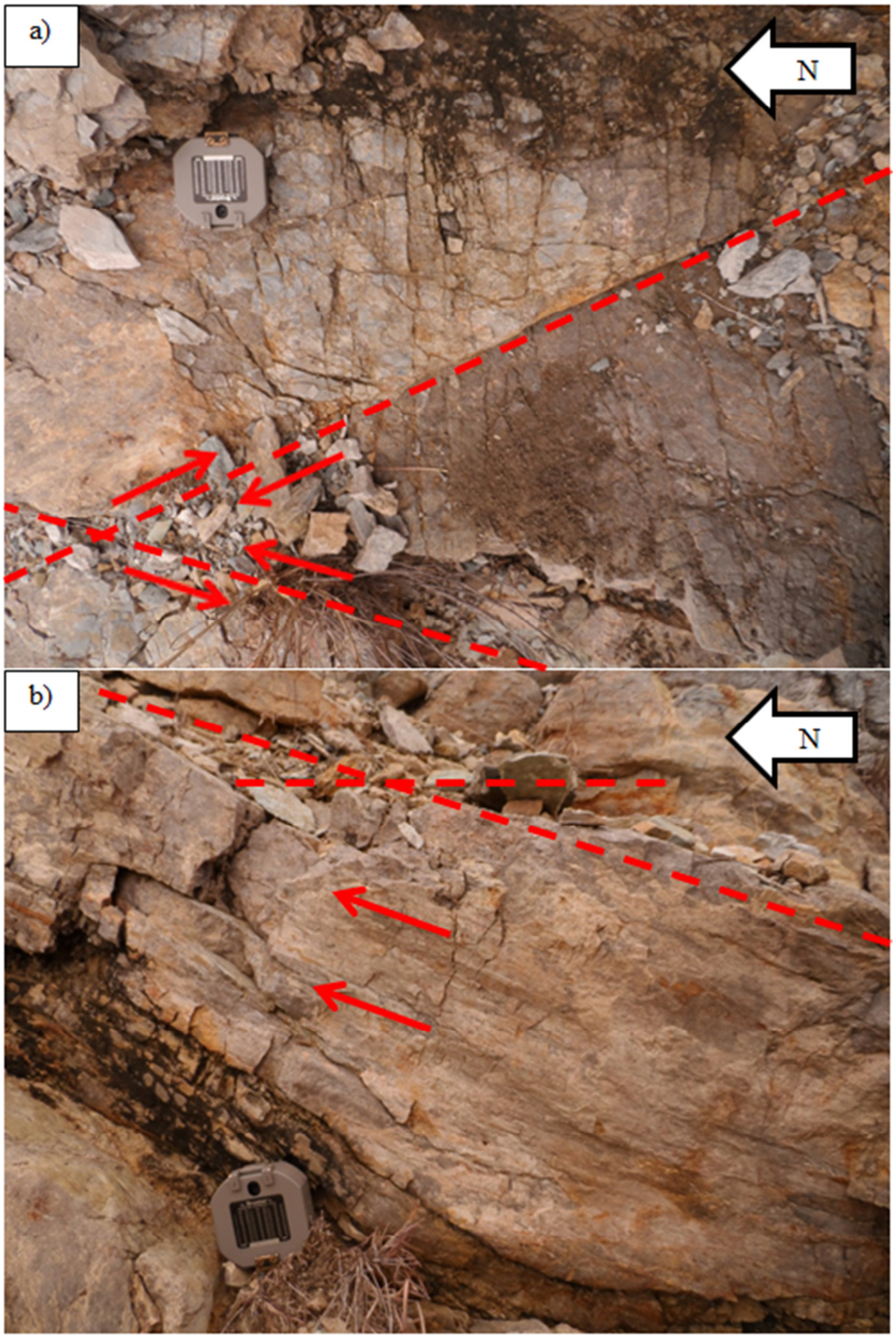

Figure 19. (a) Photo showing evidence of compressional displacement along the horizontal face of fault B. Arrows show relative displacement along faults shown by dotted lines. (b) Evidence of displacement along Fault B showing smaller scale vertical strike slip faults along includes stepping and slickensides. Arrows show relative displacement along face of fault.

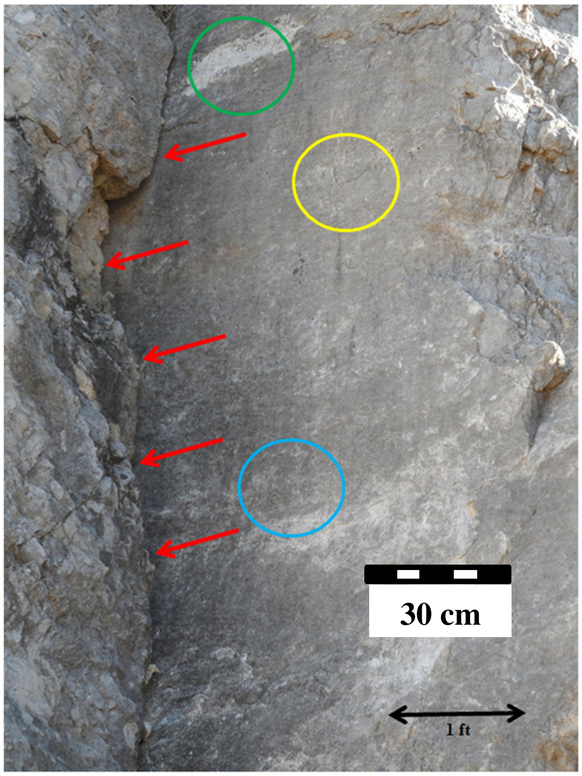

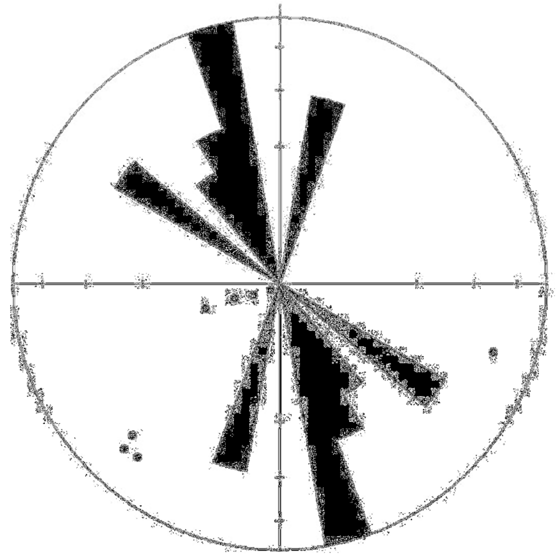

Figure 20. Upper hemisphere Rose Diagram and Schmidt Plot of the strike and dip of faults observed in the study outcrop.

Figure 21. Photo of fault H. Red arrows show direction of displacement of the fault block pictured on the right. Evidence for the displacement is the right facing steps (yellow circle), mineralization (green circle), and striations (blue circle) along the face of the block.

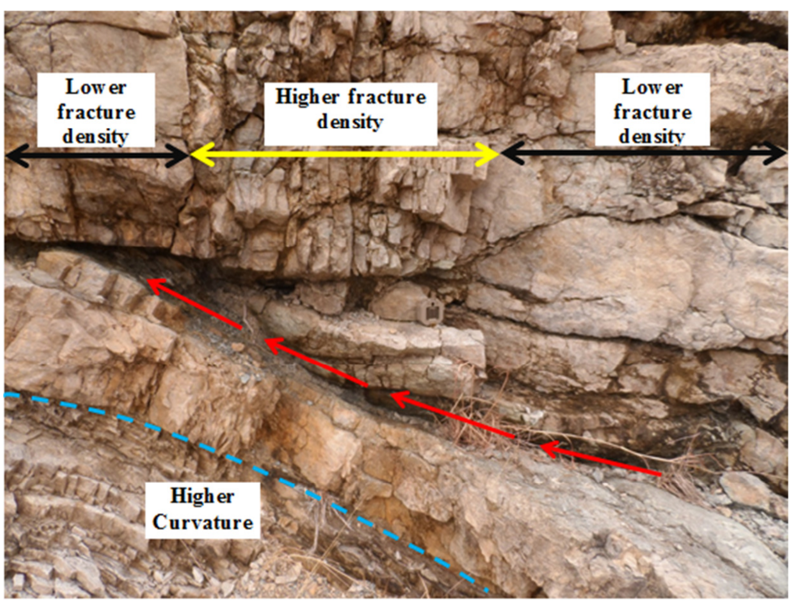

Figure 22. Area at the toe of the thrust (Fault C in Figure 17) showing transition between low and high fracture density above an area of higher curvature compared to the rest of the outcrop. Brunton compass is shown for scale.

Figure 23. Photo of an area of higher fracture density above an area of higher curvature at Fault C in Figure 23. Brunton compass is shown for scale.

Figure 24. Photo of an area of higher curvature under an area of higher fracture density at Fault C in Figure 23. Brunton compass is shown for scale.

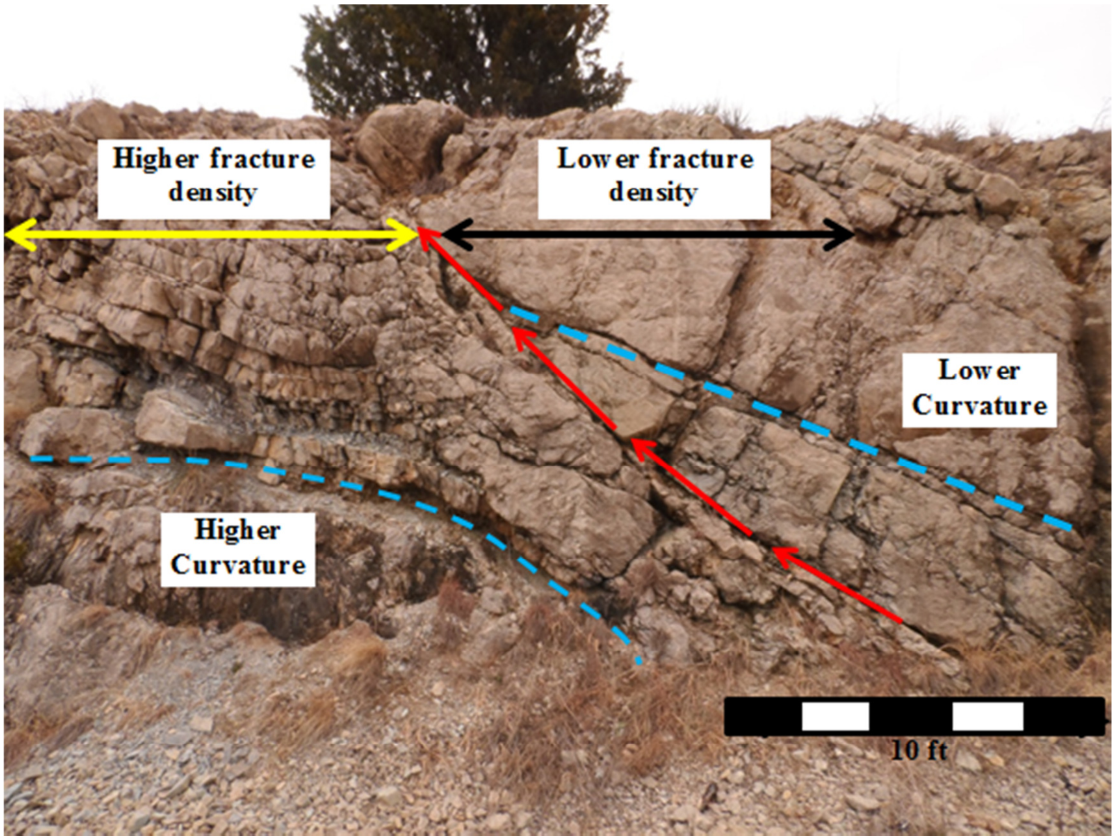

Figure 25. Photo of location 2 showing area of high fracture density above area of higher curvature. Although the beds on either side are equidistant from the fault, beds associated with higher curvature exhibited higher fracture density.

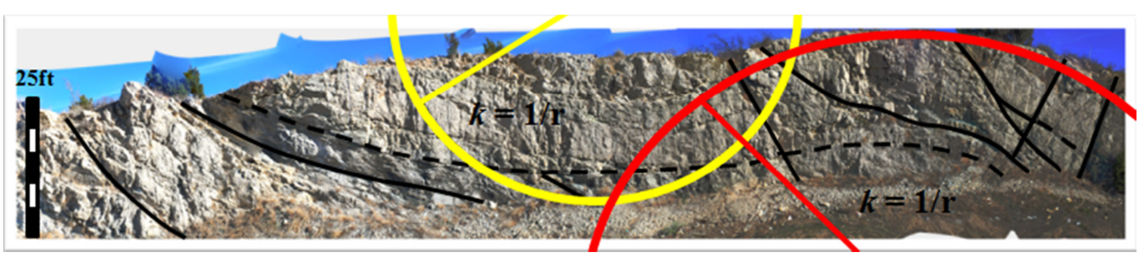

Figure 26. Outcrop photo showing how sub seismic fault displacement would reflect as positive curvature (red circle) and negative curvature (yellow circle) along structural dip.

SUBSURFACE ANALYSIS

Methodology

My dataset consists of a ~ 71 mile^2 post-stack time migrated (PSTM) 3D seismic survey and image logs from two horizontal wellbores located in Osage County, Oklahoma within the bounds of the blue rectangle in Figure 27. Prior to my study, the seismic survey was subjected to structure oriented filtering (SOF) to remove noise. The analysis included the following steps:

1. Extracting the seismic attributes of coherence, k_1 most positive curvature, k_2 most negative curvature, Euler curvature at azimuth parallel to the two wells.
2. Importing the above parameters into interpretation software along with the original seismic survey.
3. Manual picking of the Mississippian Limestone top horizon using the amplitude of the SOF seismic survey, and extracting the seismic attributes at this horizon.
4. Connecting the wells by using sonic logs from measured in depth to the seismic data time.
5. Processing the raw image log files, interpreted, and picked bedding planes, faults, and fractures.
6. Perform a qualitative correlation between fracture density and curvature values, as well as a comparison between seismic attributes and fracture orientation.
7. Using the measured bedding planes in the image logs to calculate the curvature along the borehole and compare it to the Euler curvature in the direction of the borehole from the seismic analysis.

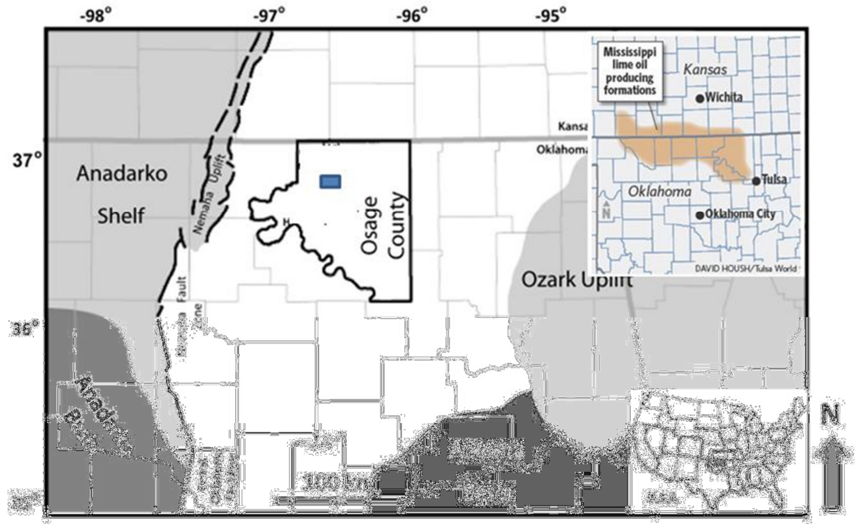

Figure 27. Location of study area (blue rectangle) within Osage County, Oklahoma, U.S.A. (After Elebiju et al., 2011; Walton, 2011).

Seismic Analysis and Interpretation

I began interpretation of the seismic data by picking the Mississippian Limestone horizon on the SOF amplitude seismic volume. The top of the Mississippian Limestone horizon is a major regional unconformity and gives rise to a strong reflection response. Figure 28 shows the resulting two way time structure map.

I used this horizon slice through the k_1 most-positive curvature k_2 most-negative curvature showing large scale regional anticlinal and synclinal features as well as fault patterns. The yellow arrows in Figures 29 and 30 indicate prominent NE-SW trending lineaments which I interpret to be left lateral wrench faults associated with the Nemaha fault system and Ouchita orogenic event in the early Pennsylvanian. Rogers (2001) notes many wrench faults and pop up blocks in north central Oklahoma associated with the Nemaha Fault system. Interpreted fault displacement terminates at the Late Mississippian-Middle Pennsylvanian unconformity which shows the deformation ended during that time (Figure 31).

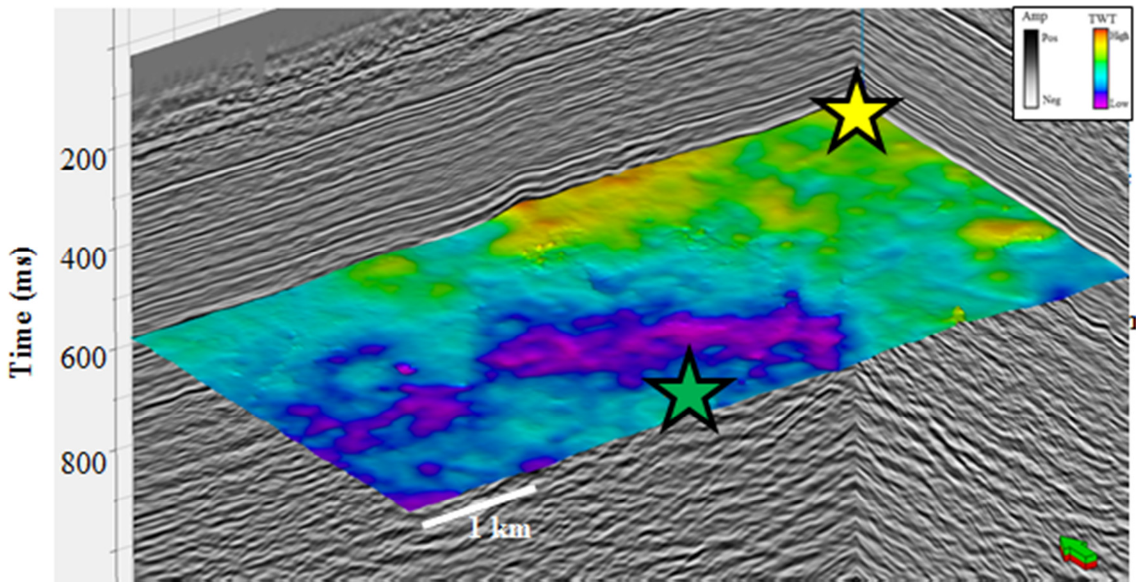

Figure 28. Two way time structure map on the top horizon of the Mississippian Limestone. Structurally high areas are in warmer colors and structurally low areas are in cooler colors. Location of well "A" is shown with yellow star and location of well "B" is shown with a green star.

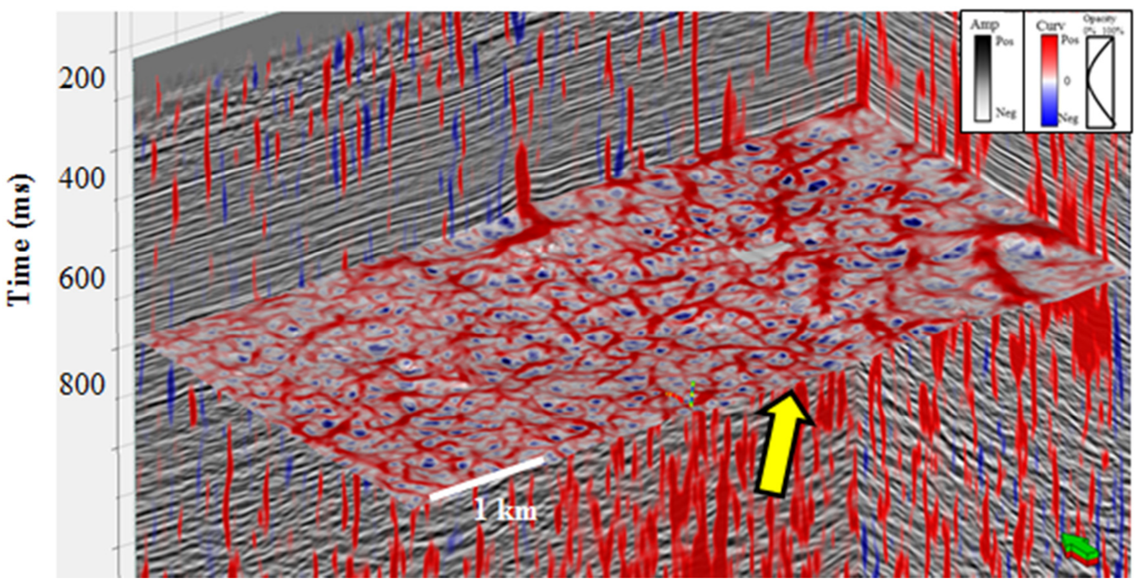

Figure 29. Horizon slice along the top of the Mississippian Limestone through the k_1 most positive curvature volume. Yellow arrow indicates a prominent NE-SW trending lineament.

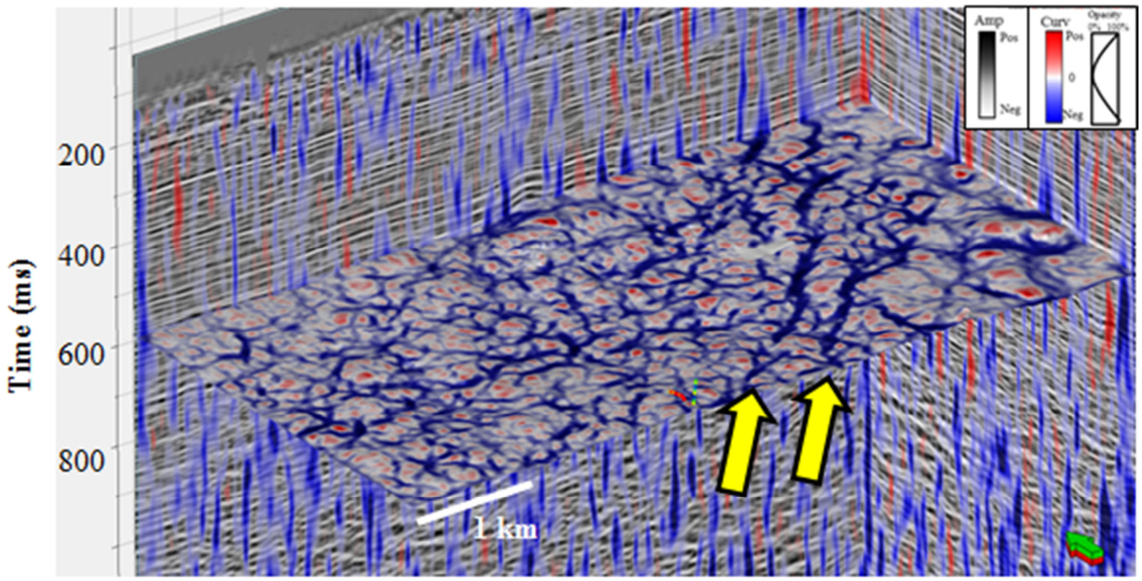

Figure 30. Horizon slice along the top of the Mississippian Limestone through the k_2 most-negative curvature volume. Yellow arrows indicate prominent NE-SW trending lineament.

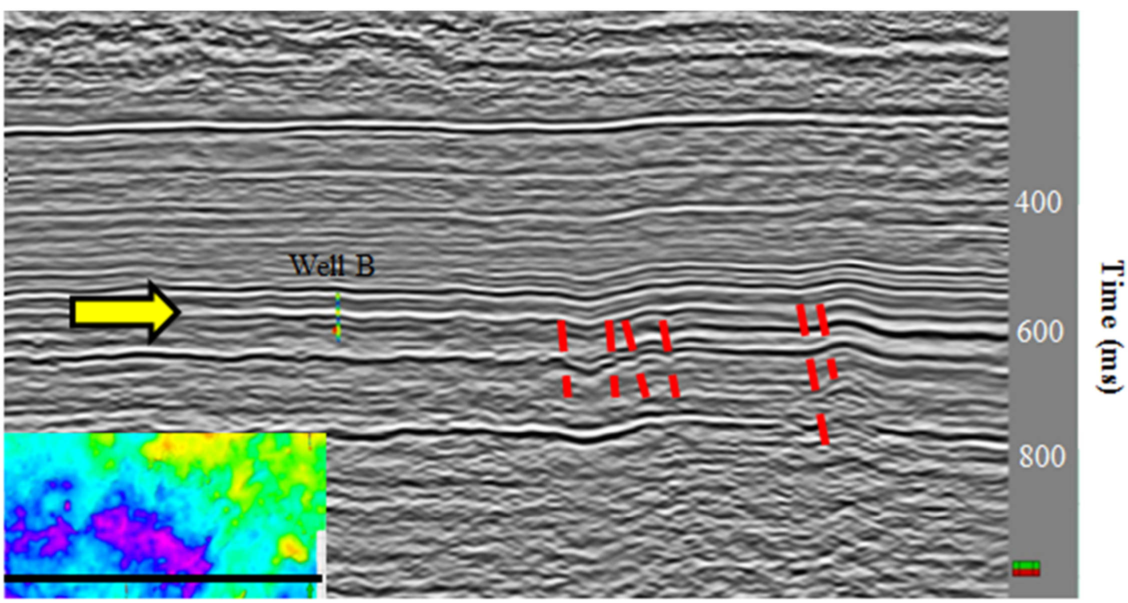

Figure 31. Vertical amplitude slice running west to east across the study area. Caption in lower left hand corner is TWT structure map with displayed vertical slice traced in black. Yellow arrow shows the top of the Mississippian Limestone. Dashed red lines are interpreted faults that correlate with NE-SW trending lineaments in curvature maps.

Image Log Analysis and Interpretation

Detection of surfaces on the image-logs

Borehole image logs allow inference of a range of subsurface features including bedding plane orientation, stress state, fracture orientation, and fracture density. The two image logs used here are from two sub-horizontal wells, referred to as A and B, located in inside the seismic survey area (Fig. 28). For the analysis, the raw data files were imported to Techlog Petrophysical Interpretation software package. Bedding surface and fractures observed as sinusoidal curves on the image logs (Figure 32) were manually picked. In image logs of sub-horizontal wells, surfaces of gentle inclination appear as high amplitude sinusoids, and vice versa for steep surfaces.

I divided the detected fractures into groups:

(1) layer bound fractures that terminate at bedding planes;

(2) layer-crossing fractures that cut across bedding planes;

(3) low resistivity fractures that appear as dark brown or black on the images; they are assumed to be fluid filled and fluid conductive;

(4) high resistivity fractures that appear on as bright yellow and are assumed to be filled by secondary mineral (quartz or calcite); they are assume to be dry with low fluid conductivity.

Quality ranking of the surfaces was based on the percentage of visibility of the sinusoidal curve: Ranking A, B, and C are for >90%, 50-90%, and <50% visibility, respectively (Figure 32).

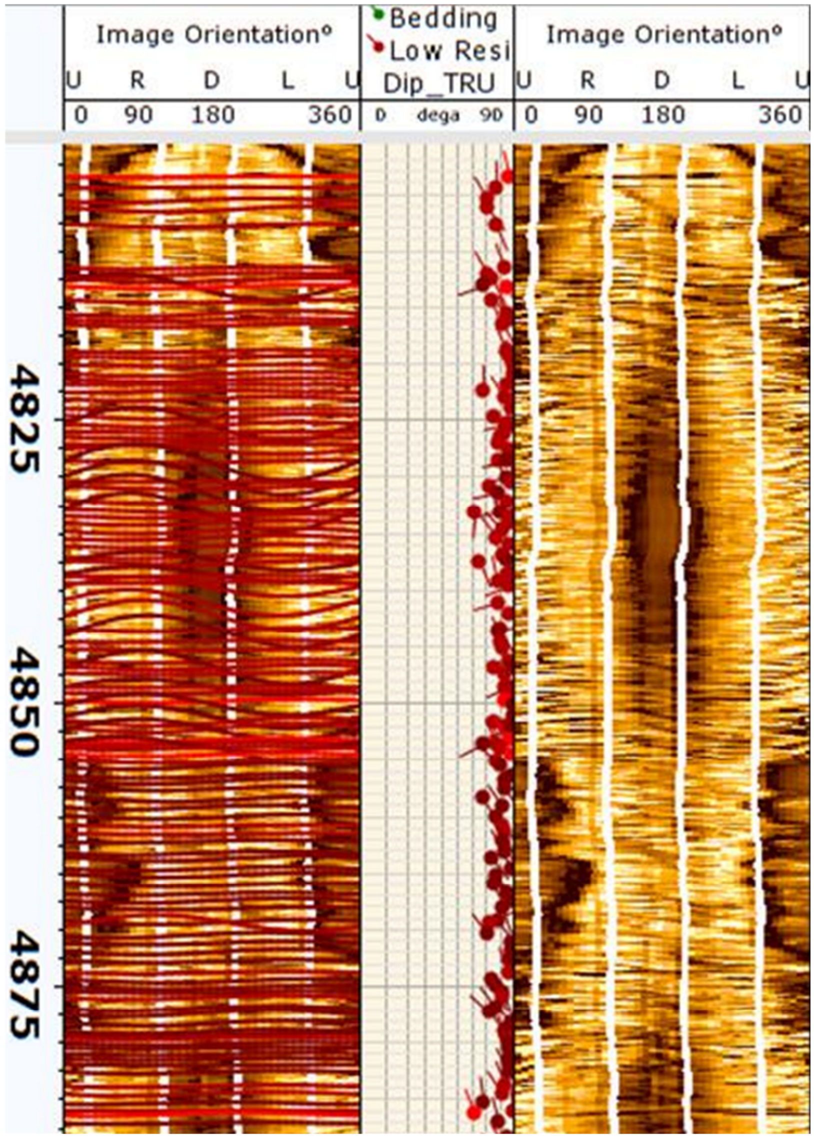

Figure 32. A fractured chert layer in the image log of Well A. Tracks from left are measured depth, the image log with interpreted fracture sinusoids, dip tadpoles from interpreted fractures, and the uninterpreted image log. All sinusoids in this example represent Layer Bound, Conductive (A, B, and C) fractures. “A” fractures are bright red and color darkens as quality decreases. Since this is an image log in a horizontal wellbore the image is taken parallel to bedding. Horizontal bedding has a high amplitude short wavelength sinusoid.

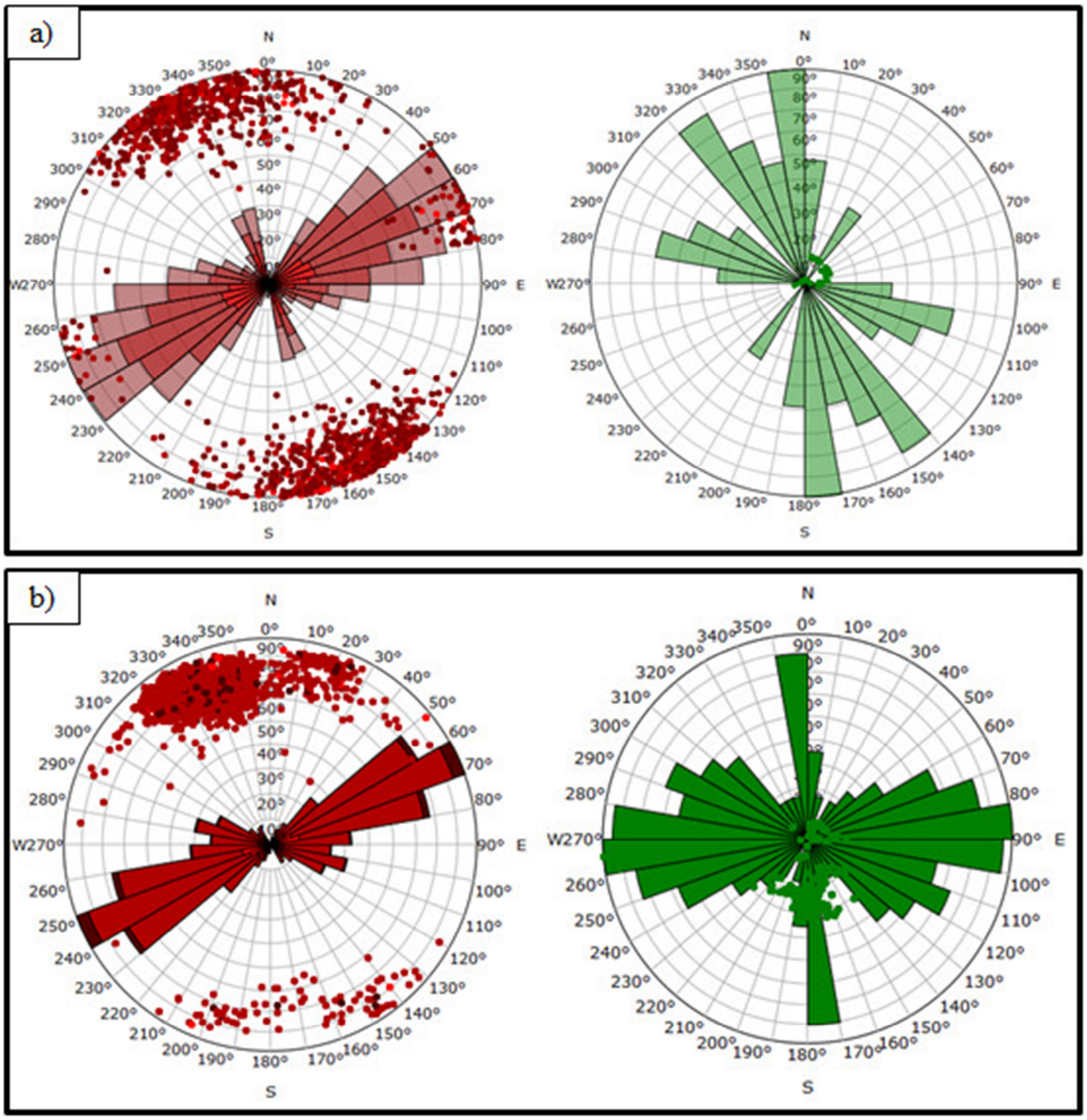

Figure 33. Upper hemisphere stereonet projections of fracture orientations (red) and bedding plane orientations (green) for well A (a) and well B (b). Strike orientations are shown using a rose diagram while dip orientations are shown

Synthesis

Stereonet projections of picked fractures and bedding surfaces are picked in Figure 33. The dominate trend of the fractures in both wells is ENE-WSW. This orientation is consistent with the direction of maximum horizontal stress in Oklahoma according to Heidbach's World Stress Map (2012) (Figure 34).

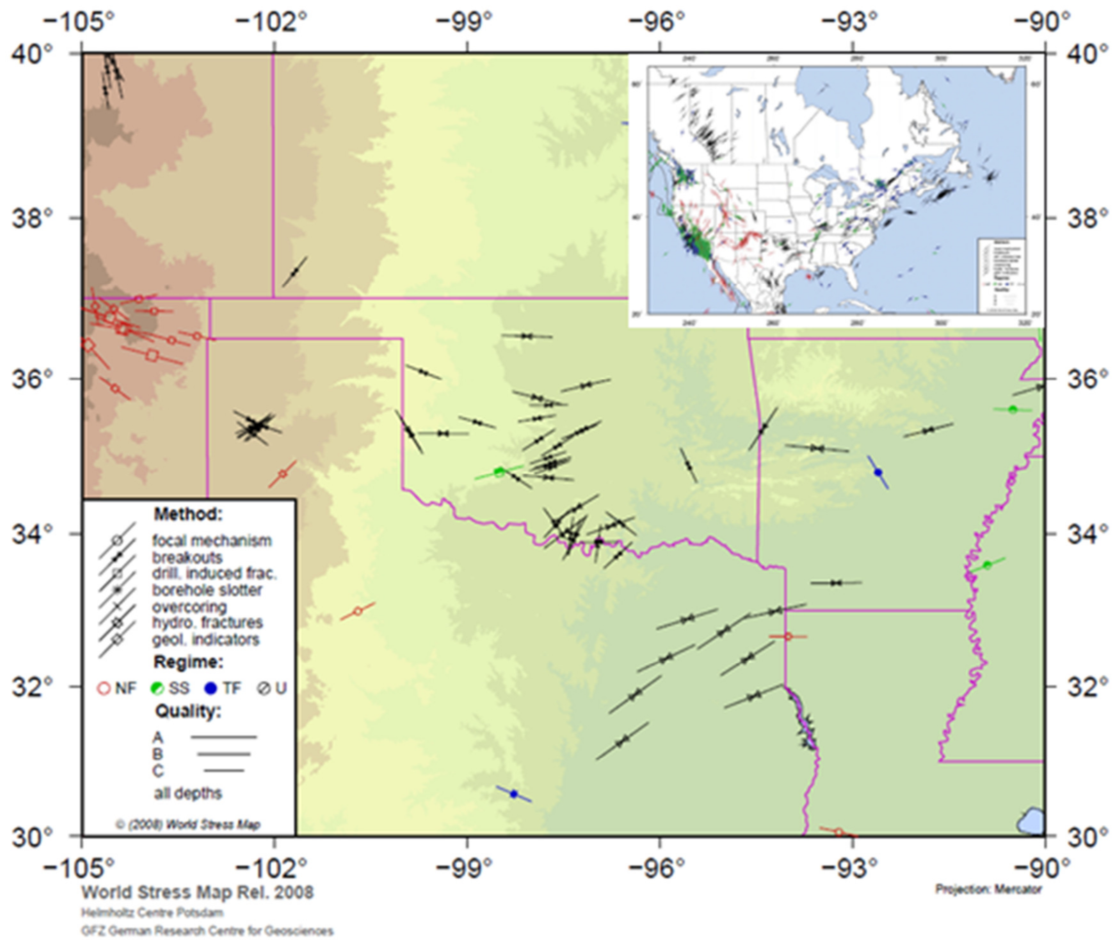

Figure 34. Map of regional stresses in the North American continent. Stress in Oklahoma is predominantly NE-SW. Heidbach's World Stress Map (2012).

Less prominent fracture sets appear in both wells. In well A this fracture set strikes approximately 90° to the predominant fracture set, and in well B strikes approximately 40° to the predominant fracture set. NE-SW fractures dip steeply in a NW-SE direction in both wells with the less prominent NW-SE set dipping NE-SW. Bedding planes are oriented primarily in a N-S pattern in Well A and an E-W pattern in Well B.

To correlate between borehole and seismic data curvatures, I calculated the structural curvature on the image logs from bedding plane orientations, and compare them to the Euler curvature in the borehole direction as determined in the 3D seismic survey. Both wells trend approximately N-S (Fig. 35). I used the rate of change (in degrees) per 13 m of length along the bedding structure for both borehole and Euler curvatures. Well A (Figure 36) shows good correlation between borehole curvature and seismic curvature in both amplitude and wavelength. Well B (Figure 37) shows a poor correlation in trend and no correlation in amplitude.

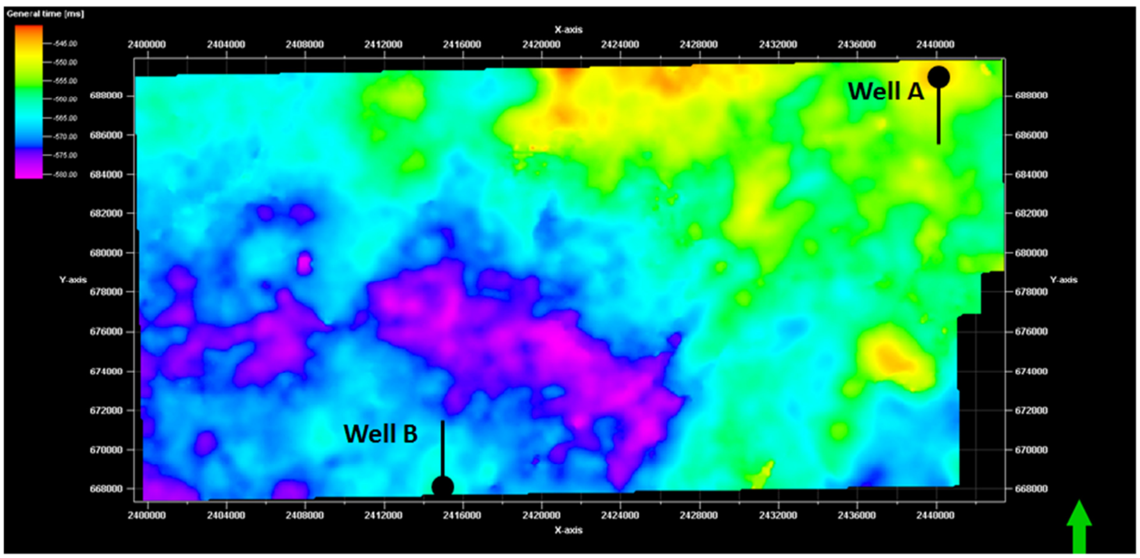

Figure 35. Time structure map on the top of the Mississippian Limestone with wells A and B projected onto the map from below. Surface locations are shown by circles and lateral wellbores are shown black lines. Structurally low areas are shown in cooler colors like blue and purple while structurally high areas are shown in warmer colors like yellow and red.

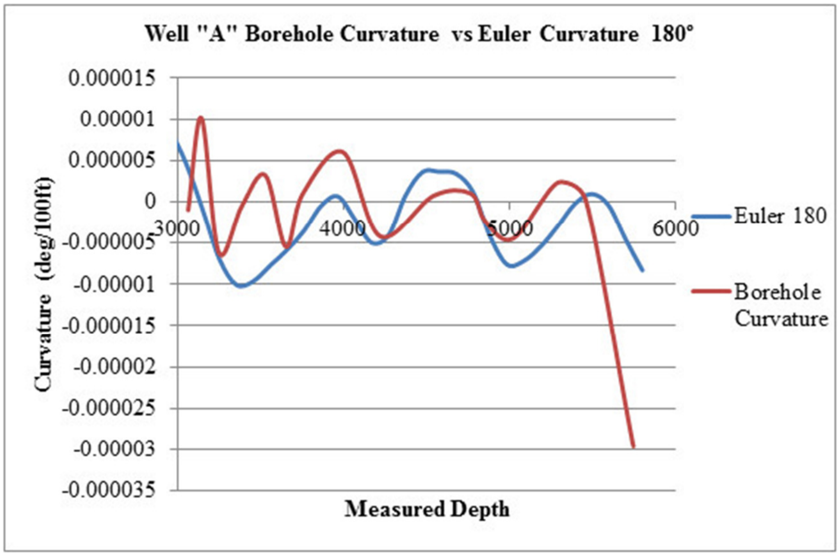

Figure 36. Well "A" borehole curvature vs Euler curvature at 180°. Borehole curvature has a similar trend and amplitude to Euler curvature.

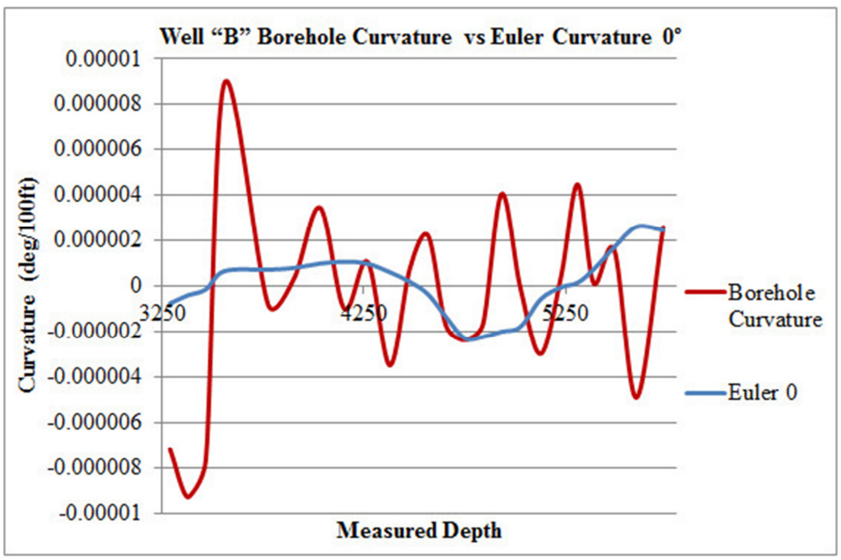

Figure 37. Well "B" borehole curvature vs Euler curvature at 0°. Borehole curvature has a similar trend to Euler curvature but no correlation with amplitude.

Correlation of seismic attributes to image logs observations

I used the Terghazi method, which compensates for fracture orientation, to calculate fracture density; the calculations are for a 13 m window size, and a 6 m step size to facilitate the comparison between image fracture density and the seismic scale. I produced a LAS file using Techlog software package which was then imported into the interpretation software along the wellbore deviation pathway.

Next, I examine fracture density's correlation with k_1 most-positive curvature and k_2 most-negative curvature. Figures 38 and 40 show fracture density displayed as a 3-D pipe along the wellbore path in front of a vertical seismic amplitude slice co-rendered with curvature. Figures 39 and 41 are plots that correspond to the images in figures 38 and 40. Here, the fracture density is plotted on Y axis and well depth on the X. The data points are colored according to seismic attributes with warmer colors for highest positive curvature of k_1 (anticlines), and cooler colors for the highest positive curvature of k_2 (synclines). No correlation between high fracture density shown at points A and B and k_1 most-positive curvature exists in well A (Figure 39a). No correlation exists in well A between high fracture density at point C and k_2 most-negative curvature. A positive correlation exists in well A between high fracture density at point D and k_2 most-negative curvature at a measured depth between 4800-5300ft (Figures 39b). When the fracture density and k_2 most-negative curvature are cross-correlated an R^2 of < .01 is obtained, showing that it is not a linear relationship. Similarly, a visual correlation can made between k_1 most-positive curvature at a measured depth between 4900-5200ft in well B (Figures 40a and 41a), but again the R^2 is low with a value of .040. No correlation between high fracture density and k_2 most-negative curvature exists in well B as high curvature values appear in areas with low fracture density at a measured depth of 4000ft, and also in areas of high fracture density at a measured depth of 4650ft and 5600ft (Figures 40b and 41b).

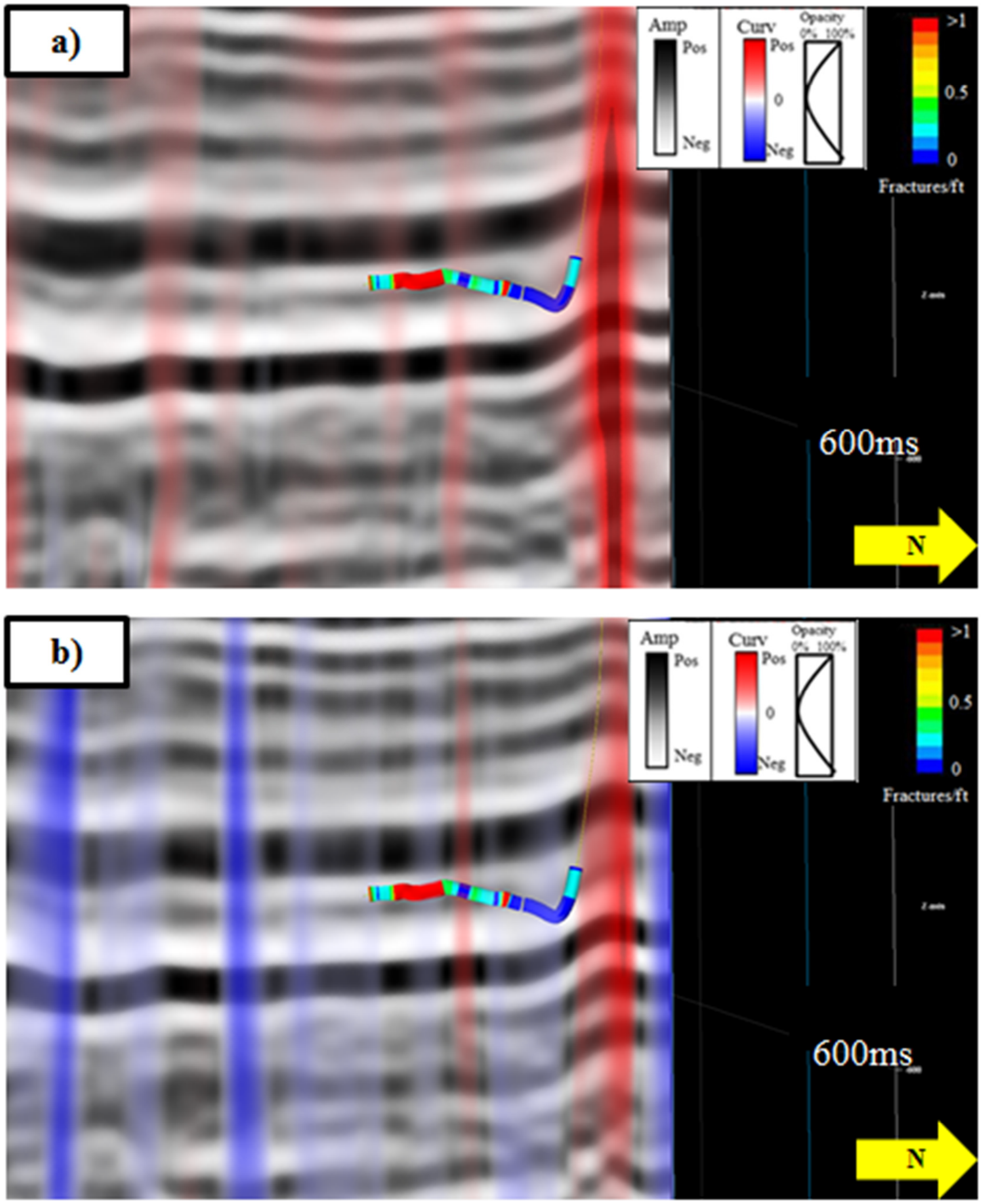

Figure 38. Fracture density from the image log displayed as a 3D pipe along the wellbore in well A. Seismic amplitude co-rendered with k1 most-positive curvature (a) and co-rendered with k2 most-negative curvature (b).

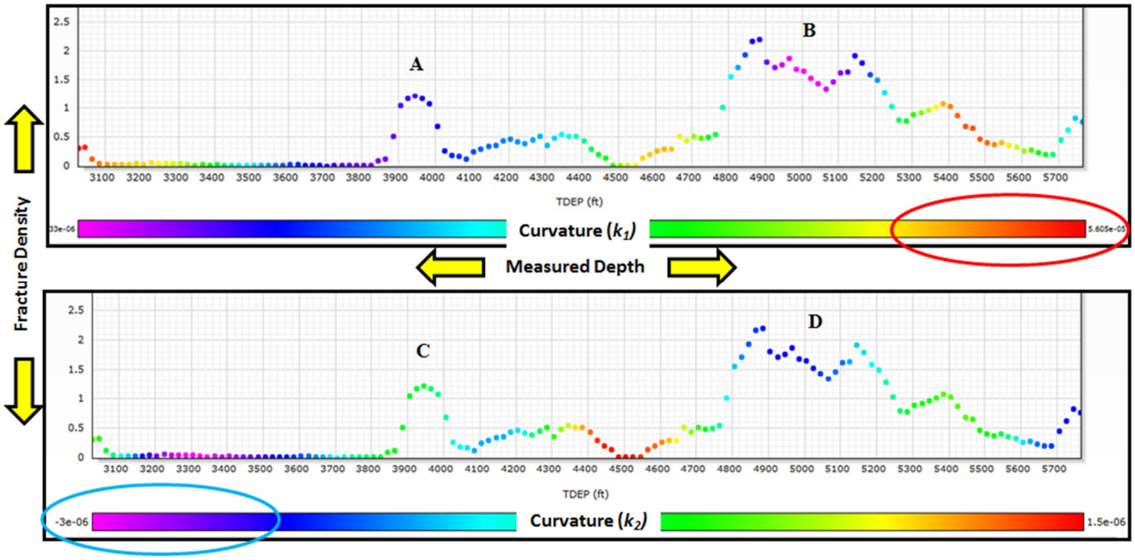

Figure 39. Walk out plots of fracture density (y axis) and measured depth (x axis) from well A colored by k_1 most-positive curvature (a), and k_2 most-negative curvature (b). In (a), fracture density shows no correlation with high k_1 most-positive curvature values shown in warmer colors. In (b), the high fracture density correlates with the higher k_2 most-negative curvature values shown in cooler colors at point D.

Correlation of Petrophysical Logs to Image Logs

Lithology is a determining factor in predicting which rocks will fracture under lower applied stresses (Nelson, 2001). Typically, it is observed that stiffer, more brittle rocks like sandstone, chert, and dolomite, fracture before more compressible ductile rocks like mudstone, siltstone, and shale (Nelson, 2001). Characteristics of primary importance when examining fractured rocks are grain size, mineralogy, and porosity (Nelson, 2001). Rocks with larger grain size, higher brittleness, and low porosity fracture at relatively lower stresses (Nelson, 2001). I estimated these properties from the logs of gamma ray, bulk density, and neutron porosity. In this series of plots I measure fracture density on the Y axis and measured depth on the X axis such that it provides a profile view along the wellbore from the heel of the well on the left to the toe of the well on the right. The data points are colored by log value.

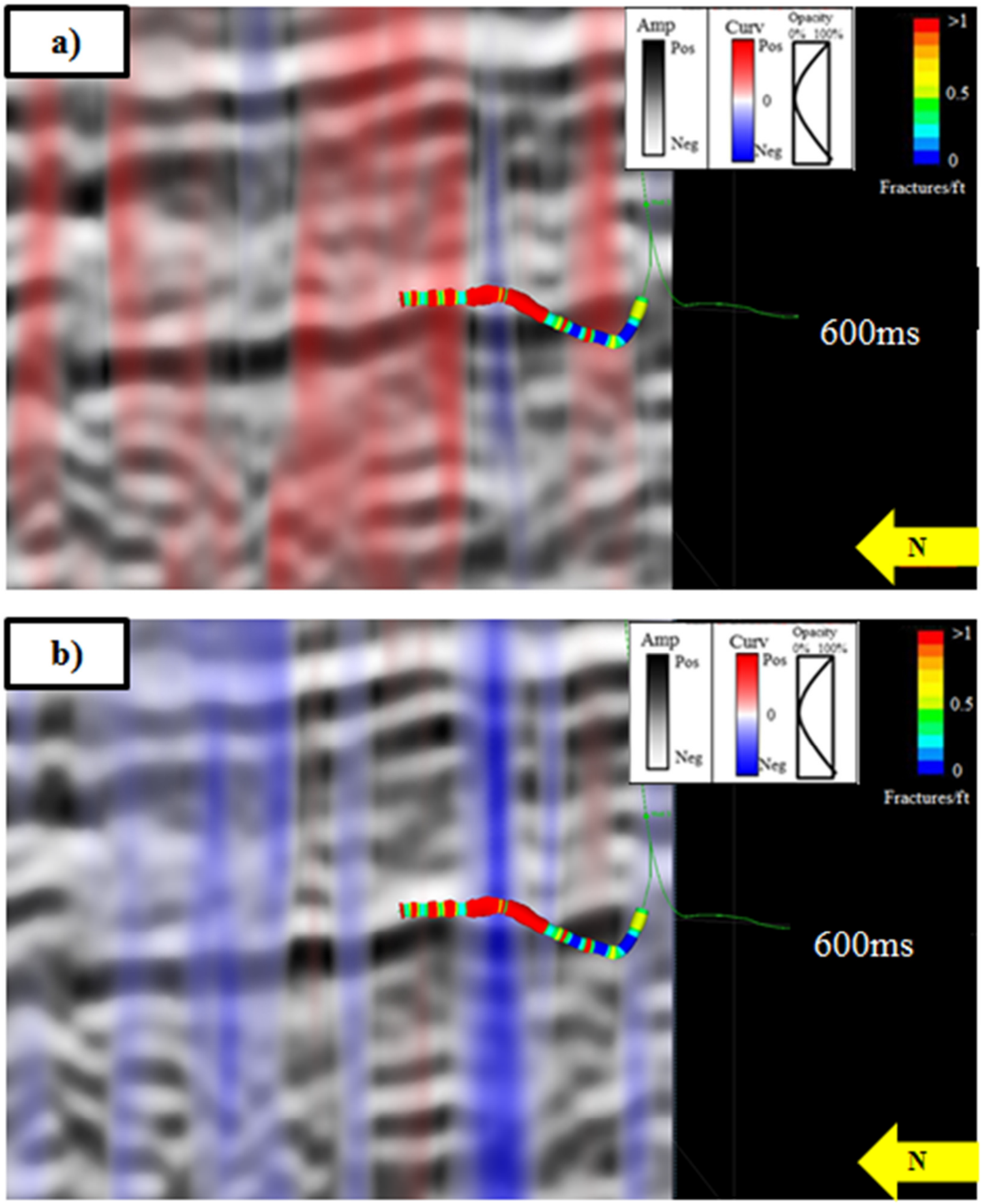

Figure 40. Fracture density from the image log displayed as a 3D pipe along the wellbore in well B. Seismic amplitude co-rendered with k1 most-positive curvature (a) and co-rendered with k2 most-negative curvature (b).

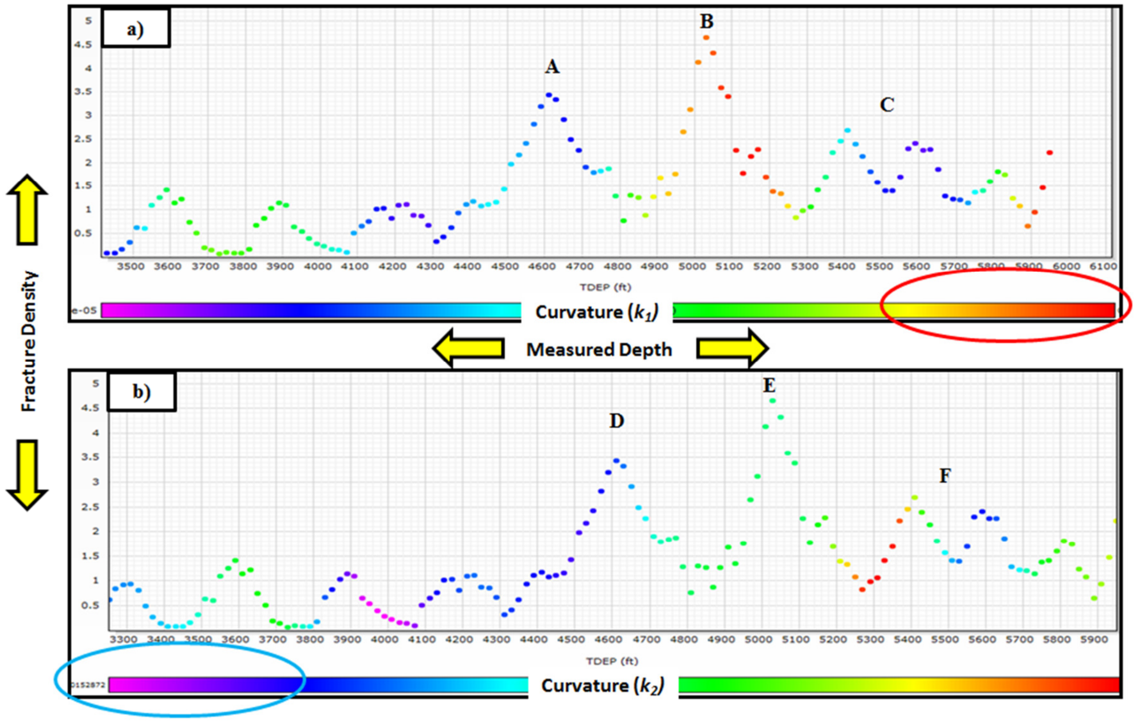

Figure 41. Walk out plots of fracture density from the image log (y axis) and measured depth (x axis) from well B colored by k_1 most-positive curvature (a), and k_2 most-negative curvature (b). In (a), the highest measured fracture density correlates with the highest k_1 most-positive curvature values shown in warmer colors. In (b), some areas of high fracture density correlate with the high k_2 most-negative curvature values shown in cooler colors.

The gamma ray comparison to fracture density (Figure 42) displays a gamma ray color bar that uses cutoffs at points between 0-150 gAPI. Points below 31 gAPI are colored in shades of blue, represent low clay volume and thus relatively more brittle; the yellow (31 - 64 gAPI), green (64 - 107 gAPI), and gray/black values (above 107 gAPI) indicate increase of clay volume and corresponding decrease of brittleness. It is expected that higher fracture density corresponds to lower clay volume (blue).

In well A (Figure 42a) segments A and B of high fracture density correlate with low gamma ray zones (< 31 gAPI). Similarly, in well B (Figure 42b), the segment of high fracture density, C, is a low gamma ray zone (< 31 gAPI). In both wells, zones of gamma ray exceeding 31 gAPI correlate with segments of lower fracture density. of fracturing. Both wells A and B show a general inverse relationship between fracture density and gamma ray intensity (Figure 43).

Figure 44 displays the relations between fracture density and neutron porosity, which is colored in a relative scale with increasing porosity from blue and purples to red-yellow-green. In both wells, the segments of high fracture density (A and B in well A and C in well B) correlate with wellbore zones of low porosity (Figure 44). The R^2 between fracture density and porosity in well A is .28 and in well B is .048 (Figure 45). However, the correlation plots of bulk density and fracture density (Figure 46) show no clear correlation (Figure 47).

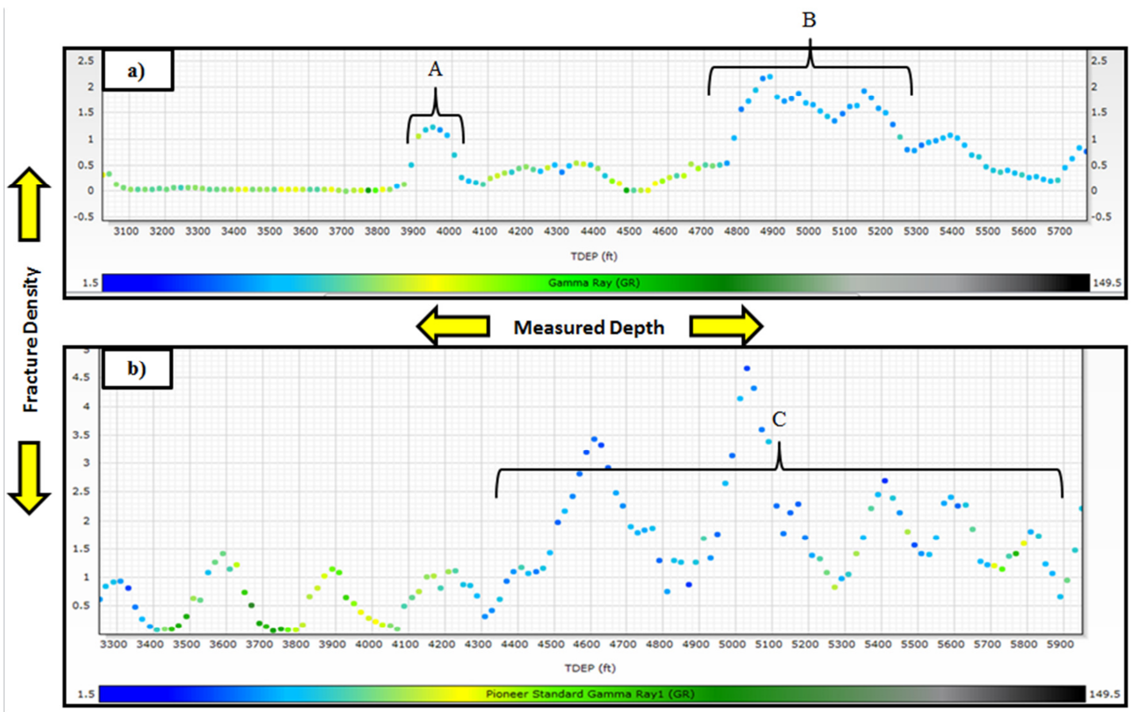

Figure 42. Walk out plots of fracture density from the image log (y axis) and measured depth (x axis) from well A (a) and well B (b) colored by gamma ray.

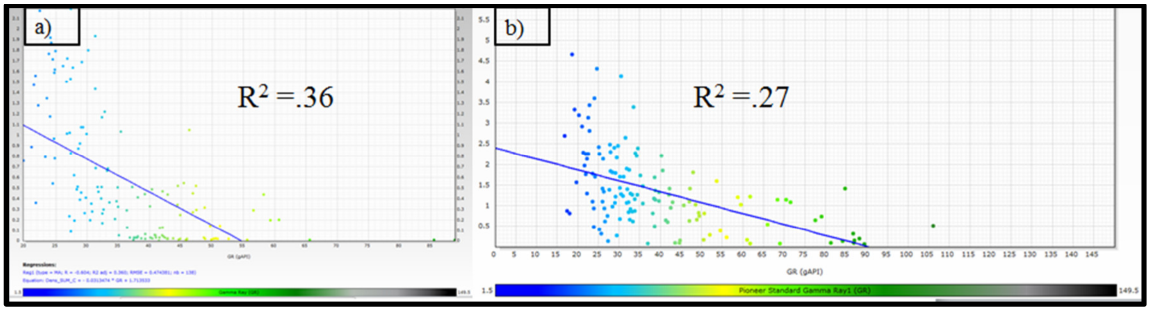

Figure 43. Cross plots of fracture density from the image log (y axis) and gamma ray (x axis) for well A (a) and well B (b). Points are colored by gamma ray.

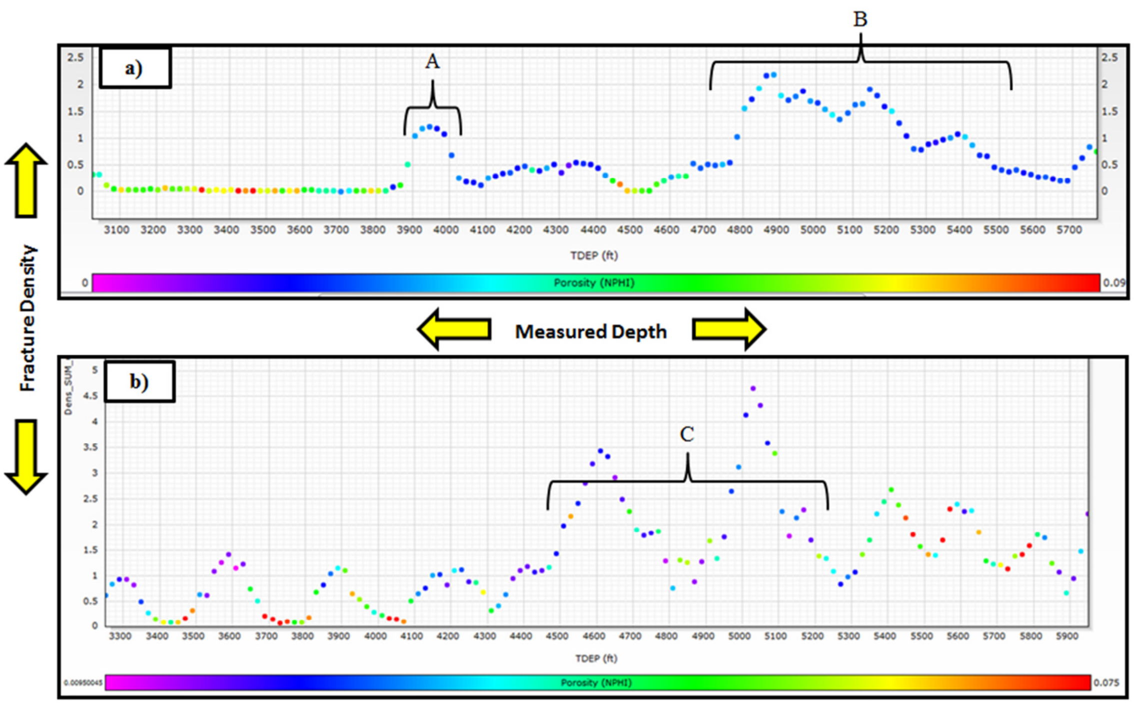

Figure 44. Walk out plots of fracture density from the image log (y axis) and measured depth (x axis) from well A (a) and well B (b) colored by porosity.

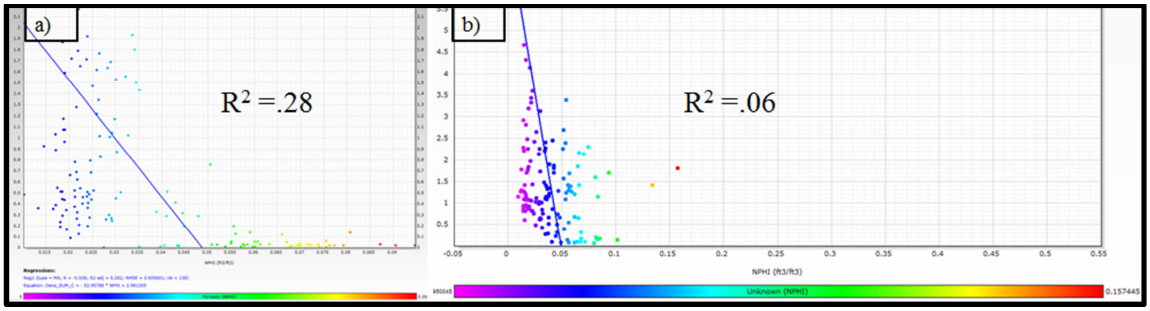

Figure 45. Cross plots of fracture density from the image log (y axis) and porosity (x axis) for well A (a) and well B (b). Points are colored by porosity.

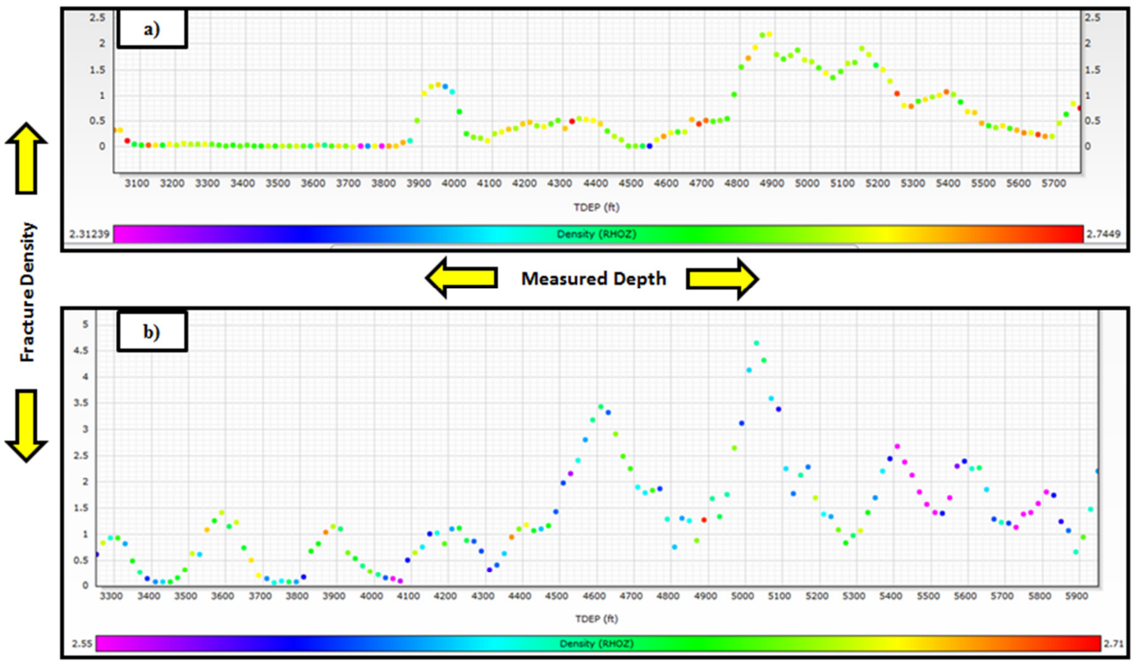

Figure 46. Walk out plots of fracture density from the image log (y axis) and measured depth (x axis) from well A (a) and well B (b) colored by bulk density.

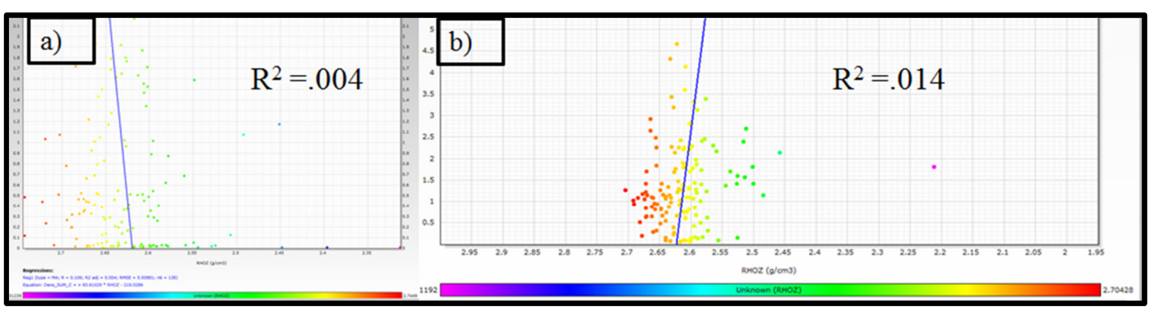

Figure 47. Cross plots of fracture density from the image log (y axis) and bulk density (x axis) for well A (a) and well B (b). Points are colored by density.

Synthesis

By definition, brittle rocks fail by fracturing when subjected to small strain (< 1%) whereas ductile rocks fail when subjected to strain > 5% (Davis and Reynolds, 2002). For this reason, in a sequence of sedimentary rocks, the competent, more brittle layers, which are composed of dolomite, chert, or limestone, are more intensely fractured than ductile, whereas less competent layers, composed of chalk or shale, are slightly or not fractured (Stearns and Friedman, 1978). In petro-physical log data, the more brittle may be recognized by low gamma-ray (less clay), and/or lower porosity (neutron) (Nelson, 2001). I found here that the segments with the highest fracture intensity, as mapped on the image logs, are strongly correlated with the low gamma ray and low neutron porosity (Fig. 42, 44). This observation indicates that lithology is the main controlling factor of fracture intensity in the Mississippi Lime in the study area. Well A provides the best support for this conclusion based on the linear correlation between fracture density and gamma ray and porosity. The situation in well B is not so clear; however it shows the possibility that high curvature values (Figure 40) could overprint the lithological controls resulting in increases of the intensity of fracturing.

CONCLUSIONS

The main conclusions of the present series of laboratory, outcrop, and subsurface analyses are the following:

(1) The clay experiments revealed that fractures can be observed only after a critical curvature, and thinner layer reached this critical stage earlier. The following curvature increase leads to quasi-linear increase of fracture intensity until

saturation stage of fracture intensity ~ 1. Subsequent curvature increase was accommodated by transferring the existing fracture into faults.

(2) The experiments displayed two scales of curvature, a regional scale, which covers the entire sample, and a local curvature, which is associated with the fracture and faults observed in clay models. This observation indicates a close association between curvature and fractures occurrence at lease in the clay models.

(3) The observations along a ~64 m outcrop, area of higher fracture density are associated with high curvature of the dolomite and limestone layers. Fracture density changed over short distances, as small as 1 ft, and thus makes the prediction of smaller scale fracture density very problematic.

(4) The Euler curvature calculated from the 3D seismic wan positively correlated with the curvature calculated from the inclination of bedding surfaces from image logs is observed in both wells. This correlation supports the use of seismic attributes to detect geologic data.

(5) Segments of high fracture intensity on the image logs are well correlated with petrophysical logs features that indicate brittleness: low gamma-ray, low neutron porosity, and high bulk density. This correlation suggests that fracture density in the Mississippian Limestone in Osage County, Oklahoma is primarily controlled by the layers lithology. The examined cores of the Mississippian Limestone support this correlation as they display that fractures preferentially occur in chert layers that fit these petrophysical logs characteristics.

REFERENCES

Al-Dossary, S., and K.J. Marfurt, 2006, 3D volumetric multispectral estimates of reflector curvature and rotation: Geophysics, **71**, P41-P51.

Blakey, R., 2011, Colorado Plateau stratigraphy and geology and global and regional paleogeography: Northern Arizona University of Geology, http://www2.nau.edu/rcb7/RCB.html, accessed 03/26/2012

Brown, W.G.; and Grayson, R.C., Jr. (eds.), 1985, Tectonism and sedimentation in the Arbuckle Mountain region, southern Oklahoma aulacogen: Baylor Geological Society and American Association of Petroleum Geologists Student Chapter, Guidebook, 44p.

Busetti, S., 2009, Fracturing of layered reservoir rocks, Ph.D. dissertation, University of Oklahoma, Norman, 272 p.

Chopra, S., and K.J. Marfurt, 2010, Integration of coherence and volumetric curvature images: The Leading Edge, **29**, 1092-1107.

Chopra, S., and K.J. Marfurt, 2007,Curvature attribute applications to 3D seismic data: The Leading Edge, **26**, 404-414.

Chopra, S., and K.J. Marfurt, 2008, Emerging and future trends in seismic attributes: The Leading Edge, **27**, 298-318.

Chopra, S., and K.J. Marfurt, 2007, Seismic attributes for prospect identification and reservoir characterization: Tulsa, Oklahoma, Society of Exploration geophysicists, 464 p.

Cloos, E., 1968, Experimental analysis of Gulf Coast fracture patterns: AAPG Bulletin, v. **52**, p. 420 - 444.

Elebiju, O.O., S. Matson, G.R. Keller, and K.J. Marfurt, 2011, Integrated geophysical studies of the basement structures, the Mississippian chert, and the Arbuckle Group of Osage County region, Oklahoma: AAPG Bulletin, **95**, 371-393.

Ericsson, J. B., H. C. McKean, and R. J. Hooper, 1998, Facies and curvature controlled 3D fracture models in a Cretaceous carbonate reservoir, Arabian Gulf, in G. Jones, Q. J. Fisher, and R. J. Knipe, eds., Faulting, fault sealing and fluid flow in hydrocarbon reservoirs: Geological Society (London) Special Publication **147**, p. 299 - 312.

Fischer, M. P., and Wilkerson, M. S., 2000, Predicting the orientation of joints from fold shape: Results of pseudo three-dimensional modeling and curvature analysis: Geology, v. **28**, p. 15 - 18.

Hart, B. S., and R. Pearson, 2002, 3-D seismic horizon-based approaches to fracture-swarm sweet spot definition in tight-gas reservoirs: The Leading Edge, **21**, 28-35.

Hart, B. S., 2006, Seismic expression of fracture-swarm sweet spots, Upper Cretaceous tight-gas reservoirs, San Juan Basin: AAPG Bulletin, v. **90**, p. 1519 - 1534.

Heidbach, O., Tingay, M., Barth, A., Reinecker, J., Kurfeß, D., and Müller, B. (2008): *The release 2008 of the World Stress Map* (available online at www.world-stressmap.org).

Hennings, P.H., J.E. Olsen, and L.E. Thompson, 2000, Combining outcrop data and 3D structural models to characterize fractured reservoirs with outcrop fracture and fault data for reservoir characterization: AAPG Bulletin, **84**, 830-849.

Hildebrand-Mittelfeldt, N., 1979, Deformation near a fault termination, Part I. A fault in a clay experiment: Tectonophysics, v. **57**, p. 131-150.

Hoppener, R., E. Kaltoff, and P. Schrader, 1969, Zur phsikalischen Tektonik: Bruchbildung bei verschiedenen Defor,ationen in Experiment. Geol. Rundsch., **59**: p. 179-193

Hunt, L., S. Chopra, S. Reynolds, and S. Hadley, 2009, On Calibrating Curvature Data to Fracture Density: Causes: CSEG Recorder, **34,** p. 27-32.

Hunt, L., S. Reynolds, T. Brown, S. Hadley, H. James, Jon Downton, and S. Chopra, 2010, Quantitative estimate of fracture density variations in the Nordegg with azimuthal AVO and curvature: a case study: The Leading Edge, **29**, 1122-1137.

Johnson, K.S., 2008, Geologic History of Oklahoma, Oklahoma Geological Survey.

Bose, S., and Mitra S., 2010,Analog modeling of divergent and convergent transfer zones in listric normal fault systems: AAPG Bullitin, v. **94**, p. 1425-1452.

Lisle, R. J., 1994, Detection of zones of abnormal strains in structures using Gaussian curvature analysis: AAPG Bulletin, v. **78**, p. 1811 - 1819.

Manaker, D. M., Turcotte, D. L., and Kellogg, L. H., 2007, Damage formation associated with bending under a constant moment: Tectonophysics, v. **433**, p. 81-95.

Manger, W.L., 2012, Lower Mississippian sequence stratigraphy and depositional dynamics: Insights from the outcrops, Northwestern Arkansas and southwestern Missouri, Oklahoma Geological Survey: Mississippian Play Workshop Guidebook

Nelson, R., 2001, *Geologic Analysis of Naturally Fractured Reservoirs;* Elsevier.

Northcutt, R. A., Johnson, K. S., and Hinshaw, G. C., 2001, Geology and petroleum reservoirs in Silurian, Devonian, and Mississippian rocks in Oklahoma: Oklahoma Geological Survey Circular **105**, p. 1-15.

Oertel, G., 1965, The Mechanism of Faulting in Clay Experiments: Tectonophysics, v. 2, p. 343-393.

Patterson, M. S., 1978, Experimental Rock Deformation- The Brittle Field. Springer, New York, N.Y., 254 pp.

Pearce, M. A., R. R. Jones, S. A. F. Smith, and K. J. W. McCaffrey, 2011, Quantification of fold curvature and fracturing using terrestrial laser scanning: AAPG Bulletin, **95**, 771-794.

Reches, Z., and D. A. Lockner, 1994, Nucleation and growth of faults in brittle rocks: AGU Journal of Geophysical Research, **99**, p. 159-173.

Reches, Z., 1988, Evolution of fault patterns in clay experiments: Tectonophysics, v. **145**, p. 141-156.

Reches, Z., Sagy, A., Roman I., 2000. Dynamic fracturing: experimental observations of dynamic fracturing in a layered sample, http://earth.es.huji.ac.il/reches/dynamic/

Reeves, T.K.,W.I. Johnson, G. Guo, B. Sharma, K.C. Chen, H.B.Carroll, 1995, Exploration 3D seismic field test/native tribes initiative: U.S. Department of Energy.

Roberts, A., 2001, Curvature attributes and their application to 3D interpreted horizons: First Break, **19**, 85-99.

Rogers, S.M., 2001, Deposition and diagenesis of Mississippian chat reservoirs, north-central Oklahoma: AAPG Bulletin, **85**, 115-129.

Sagy, A., and Z. Reches, I. Roman, 2001, Dynamic Fracturing: field and experimental observations: Journal of Structural Geology, v. **23,** p. 1223-1229.
Sagy A., and Z. Reches, 2006, Joint intensity in layered rocks: The unsaturated, saturated, supersaturated, and clustered classes. Isr. J. Earth Sci. **55**: 33-42.
Sigismondi, M. E., and J.C. Soldo, 2003, Curvature attributes and seismic interpretation: Case studies from Argentina basins: The Leading Edge, **22**, 1122-1126.
Singleton, S., and Keirstead, R., 2011, Calibration of prestack simultaneous impedance inversion using rock physics: The Leading Edge, v. **30**, p. 70-78.
Staples, E., 2011, Subsurface and experimental analysis of fractures and curvature: M.S. Thesis, U. of Oklahoma.
Stearns, D. W., 1978, Faulting and forced folding in the Rocky Mountain foreland, in Matthews, V. (ed.), Laramide folding associated with basement block faulting in the western United States: Geological Society of America Memoir 151, p. 1_37.
Tchalenko, J.S., 1970, Similarities between shear zones of different magnitudes. Geol. Soc. Am. Bull., **81**: p. 1625-1640.
Tearpock, D.J., and R.E. Bischke, 1991, Applied Subsurface Geological Mapping, Prentice-Hall, Inc. Englwood Cliffs, New Jersey.
Van der Pluijm, B., and Marshak, S., 2004, Earth Structure, New York, WW Norton & Company, 672 p.
Watney, W.L., W.J. Guy, and A.P. Byrnes, 2001, Characterization of the Mississippian chat in south-central Kansas: AAPG Bulletin, **85**, 85-113.
Walton, R., 2011, Horizontal drilling breathes new life into Mississippi Lime oil region: TulsaWorld, http://www.tulsaworld.com/business/article.aspx?subjectid=49&articleid=20110924_49_e1_cutlin919814 , accessed 03-26-2012.
White, H., B.L. Dowdell, K.J. Marfurt, and Z. Reches, 2012, Calibration of surface seismic attributes to natural fractures using horizontal image logs, Mississippian Lime, Osage County, Oklahoma: SEG Expanded Abstract.
Wu, H., and Pollard, D. D., 1995, An experimental study of the relationship between joint spacing and layer thickness: Journal of Structural Geology, v. **17**, p. 887 – 905
Zoback, M. D., 2007, Reservoir Geomechanics, Cambridge Univ. Press, Cambridge, U.K.

APPENDICIES

Appendix A: Geologic Setting

Strat*i*graphy

During the Mississippian Period, the study area of Osage County, Oklahoma, was a broad carbonate shelf environment covered by a shallow sea, similar to the present day Bahamas Shelf (Manger, 2012). It was located ~20° south of the equator (Figure 48). The sequence of the Mississippian Limestone belongs to a third order (unconformity-bounded), transgressive-regressive eustatic cycle out of four total episodes of transgression-regression during the Paleozoic (Manger, 2012).

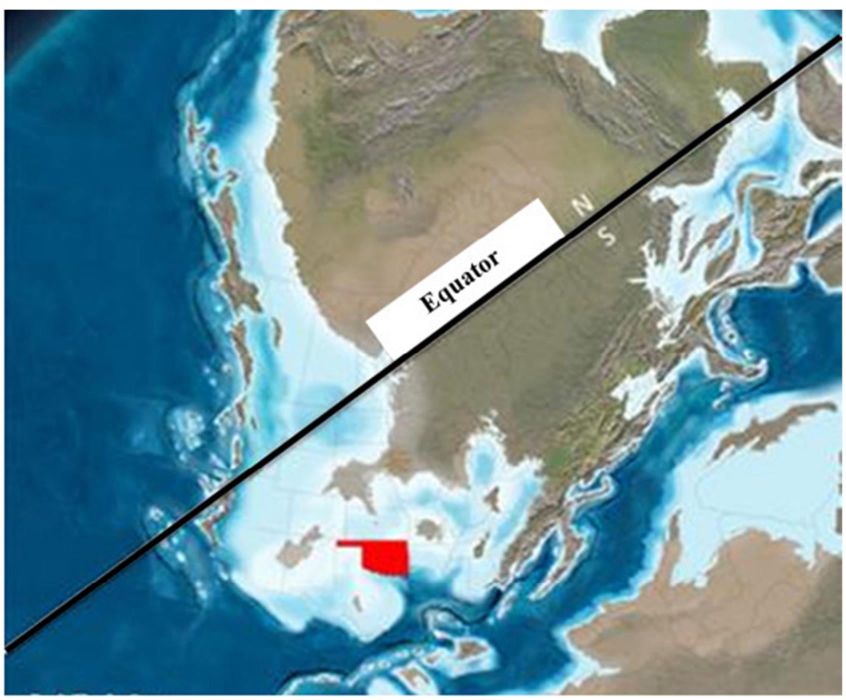

Figure 48. Paleogeographic map showing the location of North America during the Osagean, ca. 345 Ma, with the equator shown by a solid black line and Oklahoma to the south of the Equator in red. (After Blakey, 2011).

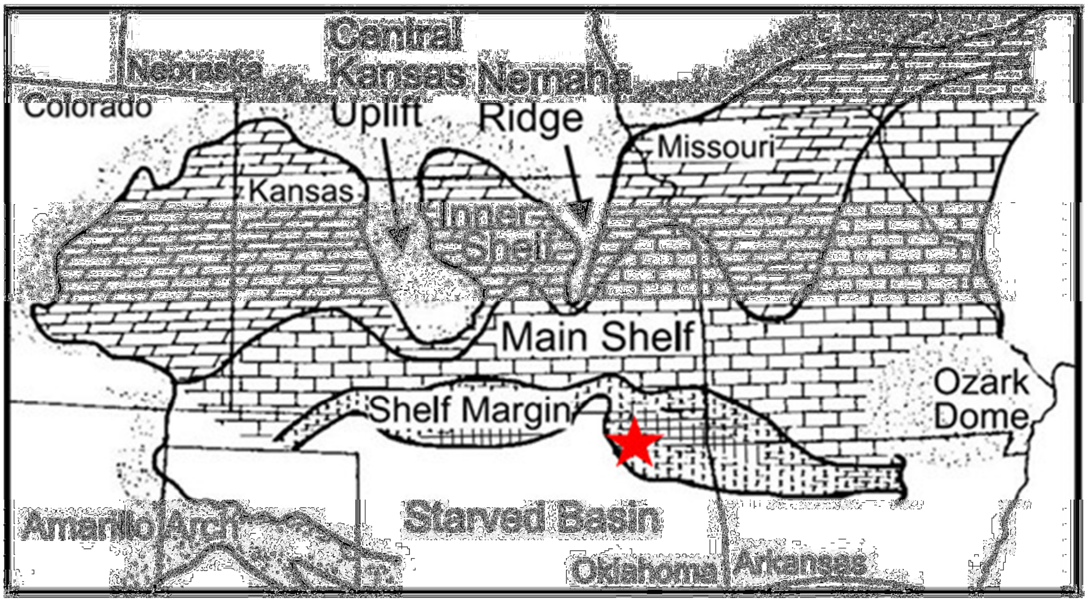

Figure 49. Paleogeographic map during the Osagean (ca. 345 Ma) showing location of carbonate shelf. Red star denotes study area (After Watney et al., 2001).

The carbonates of this sequence were transported down-ramp as lobate bodies and grain flows, and deposited below effective wave base (Manger, 2012). The Lower Mississippian unit, which is known as the St. Joe Formation, is a tight limestone having less than 6% porosity (Manger, 2012). It was deposited at high rates below effective wave base in an impoverished, cratonic, carbonate factory dominated by crinozoa detritus and carbonate mud (Manger, 2012). In the subsurface, this chert free zone is dolomitized, and exhibits some matrix porosity, whereas in outcrops it is mud dominated and tight (Manger, 2012). A stratigraphic column of the area is displayed in Figure 50.

Above the St. Joe Formation lies a chert bearing interval of the Boone Formation that in outcrops represents the maximum flooding and highstand/regressive portions of the of the eustatic cycle (Manger, 2012). The chert is formed both penecontemporaneously and through diagenetic from meteoric groundwater during prolonged subareal exposure (Manger, 2012). This diagenetic chert is the tripolite that composes the highest producing hydrocarbon reservoirs in the Mississippian Lime play. Matrix porosity in the tight limestone is approximately 5%, whereas the chert porosity is from fracture swarms occurring, and ranges up to 1%.

Informally called “chat”, the main reservoir is the “chat” at or slightly below the Mississippian-Pennsylvanian boundary (Rogers, 2001). The Mississippian Chat is a driller’s term used to describe tripolitic chert comprising the top 50-100 ft of the 300-600 ft Mississippian Limestone formation. The “chat” was formed either by in-situ diagenetic silica replacement of limestone by meteoric water during subareal exposure in the Pennsylvanian, or by redeposition of eroded material in structurally lower depocenters (Rogers, 2001). Matrix porosity in the Mississippian Chat ranges from 3-35% and its properties and thickness can vary greatly laterally, often within a few hundred feet.

Tectonics

The study area is in the Cherokee Platform that lies between the Nemaha Ridge to the west and the Ozark Plateau to the east (Figure 49). Analysis of subsurface structural maps (well logs) suggests that the local tectonic activity began in the late Mississippian, and continued into the Pennsylvanian, at least through the deposition of the Oswego limestone (Desmoinesian) (Rogers, 2001). There are a series of NE-SW trending transpressional faults relating to the Nemaha Uplift and Ouachita orogeny during the Pennsylvanian. The Ouchita orogeny resulted from the collision of Gondwana and Laurentia during the Pennsylvanian (interpretation in Figure 48), yet tectonic pulses are evident as early as the Late Mississippian (Johnson, 2008). The structurally highest areas on the upthrown side of these transpressional faults have no Mississippian units that were truncated; topographically lower areas were likely the depocenters for eroded material away (Rogers, 2001). The present day direction of maximum horizontal stress is NE-SW and is perpendicular to the opening of the ocean floor along the Mid Atlantic Ridge (Zoback, 2007).

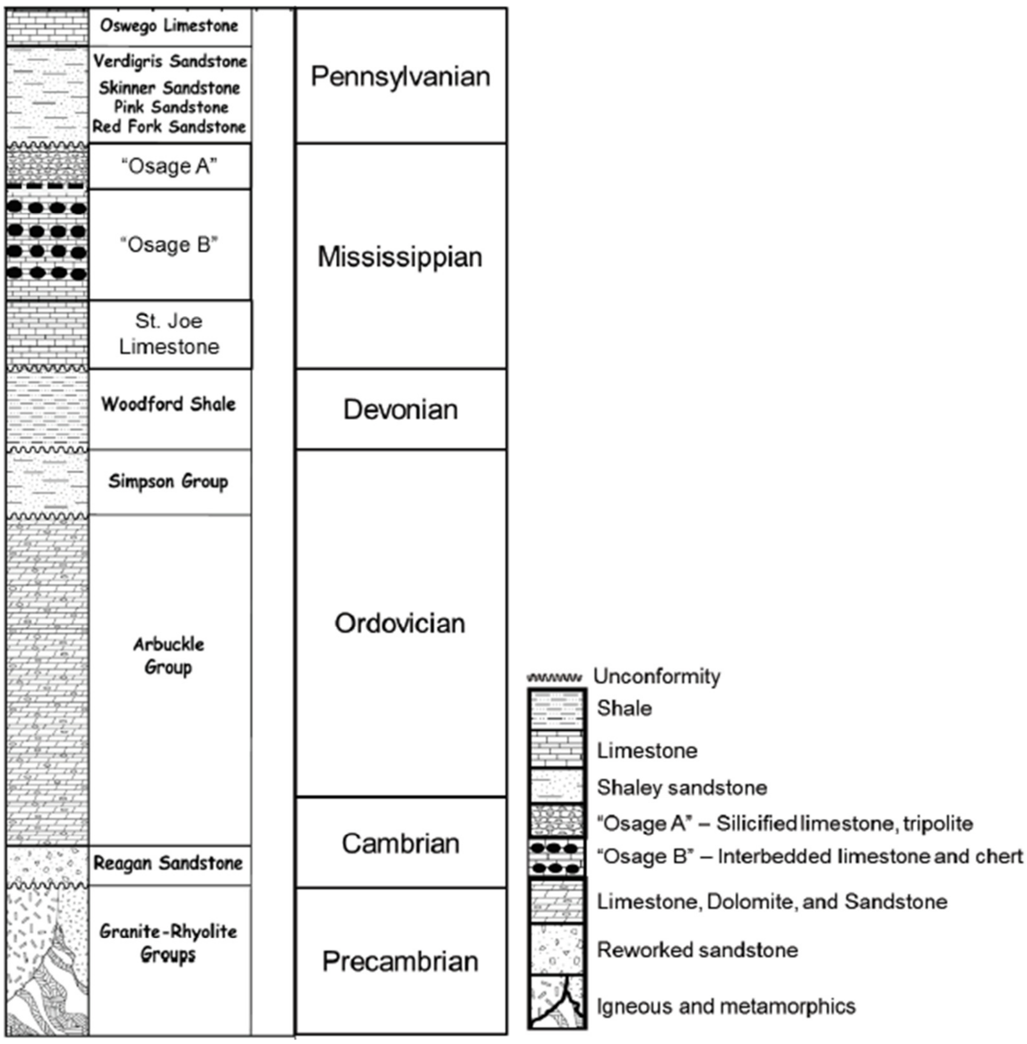

Figure 50. Generalized stratigraphic column for Osage County. "Osage A" is a silicified limestone with high diagenetic susceptibility, and is where tripolite most commonly occurs. "Osage B" contains interbedded tight, fractured

limestone and chert and has low diagenetic susceptibility. The St. Joe Limestone is the basal unit of the Mississippian in Osage County and contains no chert. (After Dowdell, 2012).

Appendix B: Core description

I examined three Mississippian Limestone cores, with total length of 45.72 m, from the Oklahoma Petroleum Information Center, Norman; no cores are available from the wells used in the study. The Lohman-2 well is a Mississippian Chat core and located within the boundaries of the seismic survey in Township 28N and Range 7E. The Chapman-Barnard 14 well is a Mississippian Chat/Limestone core from the Boone Formation and the Chapman-Barnard 24 well core is from the underlying tight St. Joe Mississippian Limestone. Both Chapman-Barnard cores are outside the study area, but close to the seismic survey in the adjacent range to the east, Township 28N and Range 8E. The cores were photographs at intervals of facies and/or lithology changes; XRD analysis was conducted on 3 samples.

The oldest examines part is the Mississippian Limestone the St. Joe Fm. which is the basal member of the Mississippian Limestone. It is a tight limestone, often oolitic, and chert free; see photos (Figure 51) from the Chapman-Barnard 24 well at 2642 ft. The core has sub-horizontal stylolites, a few of which appear to be mineralized, but none appears open, conductive features. The XRD analysis shows the mineralogy to be primarily MgCal/dolomite with less than 50% quartz (Table 4).

The examined part of the Boone Formation consists of penecontemporaneously deposited chert and tight limestone; photo (Figure 52) from the Chapman-Barnard 14 well at 2582 ft. These chert layers display a high density of layer bound hairline microfractures that terminate at the boundary between the dark gray chert nodules and the lighter interstitial silica matrix. The XRD analysis shows the mineralogy to be 95% quartz (Table (4).

The examined part of the top of Boone Fm. is diagenetically altered to silica from limestone by meteoric groundwater due to subareal exposure (Rogers, 2001); photos (Figure 53) are from the Chapman-Barnard 14 well at 2521 ft. The core fabric is sub angular suggesting that the lighter nodules were replacing the matrix. The fractures in silica nodules terminate at the calcite/dolomite matrix. The XRD analysis shows the mineralogy to be 54% quartz and 46% calcite/dolomite (Table 4). The presence of fractures is associated with as the quartz increase (Table 4) suggesting that the fracturing in the Mississippian Limestone is lithologically controlled, and may be related to amount of quartz content.

The core in Figure 53 is an example of hydrocarbon reservoir rock that is below the oil water contact. The oil stained parts in the core indicate that the oil flows though the matrix permeating into the silica nodules, yet often did not saturate all the way to the center. This suggests a greater porosity in the matrix than in the nodules possibly explaining the lack of through going fractures in the matrix.

Table 3. XRD results from Mississippian cores (minerals in %).

Well Name	Unit	Depth	Quartz	Calcite	Dolomite	Mg/CC	Pyrite	Other
Chapman 24	**St. Joe Fm.**	**2642**	**44**	**0**	**21**	**34**	**0**	**1**
Chapman 14	**Boone Fm.**	**2582**	**95**	**0**	**0**	**0**	**5**	**0**
Chapman 14	**Miss Chat**	**2521**	**54**	**33**	**13**	**0**	**0**	**0**

Figure 51. Photo of core from St. Joe Formation of the Mississippian Limestone. Core sample was recorded as being from a depth of 2642ft in the Chapman-Barnard 24 well in Township 28N and Range 8E of Osage County, Oklahoma.

Figure 52. Photo of core from Boone Formation of the Mississippian Limestone. Core sample was recorded as being from a depth of 2582ft in the Chapman-Barnard 14 well in Township 28N and Range 8E of Osage County, Oklahoma.

Figure 53. (left) Photo of core from Boone Formation of the Mississippian Limestone. Core sample was recorded as being from a depth of 2521ft in the Chapman-Barnard 14 well in Township